Atmos. Chem. Phys. Discuss., 11, 13035–13097, 2011
www.atmos-chem-phys-discuss.net/11/13035/2011/
doi:10.5194/acpd-11-13035-2011

Atmospheric Chemistry and Physics Discussions

Determination of tropospheric vertical columns of NO_2 and aerosol optical properties in a rural setting using MAX-DOAS

J. D. Halla[1], T. Wagner[2], S. Beirle[2], J. R. Brook[3], K. L. Hayden[3], J. M. O'Brien[3], A. Ng[4], D. Majonis[1,*], M. O. Wenig[5], and R. McLaren[1]

[1]Centre for Atmospheric Chemistry, York University, Toronto, ON, Canada
[2]Satellite Group, Max Planck Institute for Chemistry, Mainz, Germany
[3]Air Quality Research Division, Environment Canada, Toronto, ON, Canada
[4]Ontario Ministry of the Environment, Toronto, ON, Canada
[5]School of Energy and Environment, City U, Hong Kong, China
[*]now at: Department of Chemistry, University of Toronto, Toronto, ON, Canada

Received: 15 March 2011 – Accepted: 12 April 2011 – Published: 27 April 2011

Correspondence to: R. McLaren (rmclaren@yorku.ca)

Published by Copernicus Publications on behalf of the European Geosciences Union.

Abstract

Multi-AXis Differential Optical Absorption Spectroscopy (MAX-DOAS) measurements were performed in a rural location of southwestern Ontario during the Border Air Quality and Meteorology Study. Slant column densities (SCDs) of NO_2 and O_4 were determined using the standard DOAS technique. Using a radiative transfer model and the O_4 SCDs, aerosol optical depths were determined for clear sky conditions and compared to OMI, MODIS, AERONET, and local $PM_{2.5}$ measurements. This aerosol information was input to a radiative transfer model to calculate NO_2 air mass factors, which were fit to the measured NO_2 SCDs to determine tropospheric vertical column densities (VCDs) of NO_2. The method of determining NO_2 VCDs in this way was validated by comparison to composite VCDs derived from aircraft and ground-based measurements of NO_2. The new VCDs were compared to VCDs of NO_2 determined via the satellite instruments SCIAMACHY and OMI, for overlapping time periods. The satellite-derived VCDs were higher by 50%, with a mean positive error of 0.5–0.9 × 10^{15} molec cm^{-2}. This last finding is different from previous studies whereby MAX-DOAS geometric VCDs were higher than satellite determinations, albeit for urban areas with higher VCDs. An effective boundary layer height, BL_{eff}, is defined as the ratio of the tropospheric VCD and the ground level concentration of NO_2. Variations of BL_{eff} can be linked to time of day, source region, stability of the atmosphere, and the presence or absence of elevated NO_x sources. In particular, a case study is shown where a high VCD and BL_{eff} were observed when an elevated industrial plume of NO_x and SO_2 was fumigated to the surface as a lake breeze front impacted the measurement site. High BL_{eff} values (∼1.9 km) were observed during a regional smog event when high winds from the SW and high convection promoted mixing throughout the boundary layer. During this event, the regional line flux of NO_2 through the region was estimated to be greater than 112 kg NO_2 km^{-1} h^{-1}.

1 Introduction

The role of nitrogen oxides in the atmosphere is paramount in atmospheric chemistry due to the deleterious effects they have on the atmosphere and biosphere. Global emissions of NO_x (NO_2 + NO) to the troposphere has been estimated to be 122 Tg yr^{-1}, with approximately 74% of these emissions from anthropogenic and biomass burning sources (Müller, 1992). In the troposphere, the main source of ground state oxygen atoms, $O(^3P)$, is the photolysis of NO_2, Reaction (R1), which subsequently reacts with molecular oxygen to form ozone, Reaction (R2), collectively the two most important reactions in the photochemical formation of ground level ozone (Finlayson-Pitts and Pitts, 1999).

$$NO_2 + h\nu(\lambda < 420\,\text{nm}) \rightarrow O(^3P) + NO \quad \text{(R1)}$$

$$O(^3P) + O_2 + M \rightarrow O_3 + M \quad \text{(R2)}$$

NO_2 is also the main precursor in the formation of key nighttime species, including the nitrate radical, NO_3, and N_2O_5. Hydrolysis of N_2O_5 on aerosols and cloud droplets to form HNO_3 and particle nitrate (McLaren et al., 2004) is thought to be the main removal mechanism for NO_x in the atmosphere at night (Dentener and Crutzen, 1993). Heterogeneous reaction of NO_2 on surfaces coated with water to form HONO at night is also known to be an important reaction in the atmosphere, as photolysis of HONO is known to be a major source of OH in the morning boundary layer (Platt and Perner, 1980), and has been estimated to contribute up to 30% of the total OH production integrated over 24 h in polluted environments (Alicke et al., 2003). For these and other reasons, measurement of NO_2 in the troposphere is important. Concentrations of NO_2 at ground level can be measured via chemiluminescence instruments and through active DOAS (Platt and Stutz, 2008). Multi-AXis Differential Optical Absorption Spectroscopy (MAX-DOAS) can also be used for the measurement of small molecules such as NO_2 and O_4 through the application of the DOAS technique to spectra of sky scattered sunlight

to identify and quantify column abundances of trace gases that have narrow band absorption structures in the near UV and Vis wavelength range (Hönninger et al., 2004). In general terms, MAX-DOAS can in principle give more information on the vertical distribution of absorbers than in-situ point source measurements. The measurement requires a less sophisticated optical system, less maintenance, and less power than comparable active DOAS systems. Typical instruments have moving telescopes or mirrors that allow the collection of scattered light from different viewing directions, defined by the elevation angle above the horizon, α, and the horizontal telescope pointing direction, β. Direct measurements are analyzed to yield slant column densities (SCDs) of trace absorbers integrated along the light path, and differential slant column densities (DSCDs) of trace gas species. DSCDs are determined by fitting all measurements ($\alpha < 90^\circ$) with zenith ($\alpha = 90^\circ$) reference spectra. These spectra, called Fraunhofer references, are used to eliminate strong solar features in the incoming spectrum, and cancel out stratospheric absorptions, allowing DSCDs to contain mainly tropospheric absorptions (Hönninger et al., 2004).

The conversion of DSCDs into vertical column densities (VCDs) is not simple because, unlike active DOAS, the exact path length for each DSCD is not known and depends on factors such as aerosol levels, clouds, albedo, the profile of the trace gases, and the location of the sun. The air mass factor (AMF) is defined as the ratio of the SCD over the VCD of a trace gas (Solomon et al., 1987; Perliski and Solomon, 1993). Radiative transfer models (RTMs) may be used to obtain AMFs based upon the above parameters. Under conditions with low aerosol, the AMF may be geometrically approximated by $1/\sin(\alpha)$ for a lower atmospheric absorber and scattering event above the absorbing layer (i.e. troposphere). However, since aerosols are present in most cases, this approximation is rarely valid, and an RTM should be used.

Spectroscopic instruments aboard satellites allow for the measurement of SCDs of trace gases (Bovensmann et al., 1999; Levelt et al., 2006). Using various algorithms, VCDs of trace gases can be determined after estimation of the AMF through radiative transfer modeling (Martin et al., 2002; Celarier et al., 2008). Satellites have the

spatial advantage of obtaining global coverage, but have the temporal disadvantage of only obtaining a daily (OMI) or slightly better than weekly (SCIAMACHY) measurement for a given location on earth. The calculation of appropriate AMFs is a major task in the retrieval of tropospheric VCDs from satellite observations, as it requires a-priori information on clouds, aerosols, ground albedo, and trace gas profile. Satellite measurements of VCDs are also averaged over large pixel sizes and thus are challenged in the detection of changes on small spatial scales.

As MAX-DOAS and satellites yield comparable information on VCDs, intercomparison between the two methods is desirable. Recent studies have attempted to validate satellite measurements with ground-based measurements (Irie et al., 2009; Chen et al., 2009). The Dutch Aerosol and Nitrogen Dioxide Experiments for Validation of OMI and SCIAMACHY (DANDELIONS) study focused on urban areas and used geometrical considerations to convert MAX-DOAS DSCDs into VCDs (Brinksma et al., 2008; Celarier et al., 2008). Results from this study indicated that satellites underpredict NO_2 VCDs. Other studies have used RTMs to determine aerosol conditions and VCDs from MAX-DOAS in both rural and urban areas, using approaches that require a-priori assumptions (Wittrock et al., 2004; Heckel et al., 2005; Irie et al., 2008; Lee et al., 2009; Clémer et al., 2010).

In this paper, a two-step approach to determine NO_2 VCDs from MAX-DOAS measurements is outlined, applied to a data set on a routine basis, and validated with other field measurements. The first step makes use of measured O_4 DSCDs and the RTM McArtim (Monte carlo Atmospheric radiative transfer inversion model) to obtain aerosol conditions for each MAX-DOAS measurement following the approach introduced by Li et al. (2010). This aerosol information is then input to McArtim for the calculation of NO_2 AMFs that are ultimately compared to the measured MAX-DOAS SCDs to obtain NO_2 VCDs. In addition to the NO_2 VCDs, aerosol optical depth (τ) values, aerosol layer heights (H_{aer}), and gas layer heights (H_{gas}) are also determined. A full description and comprehensive analysis of the methodology used is in preparation (Wagner et al., 2011).

Complex meteorological phenomena imposed by lake breezes interacting with anthropogenic sources are known to modify the air quality in southern Ontario (Reid et al., 1996; Hastie et al., 1999; Sills et al., 2011). One goal of the 2007 Border Air Quality and Meteorology Study (BAQS-Met) was to examine such interactions, using a 3-week dataset collected in a rural region of southwestern Ontario, supported by ground-based and aircraft-based measurements of trace gases and aerosols. The methodology outlined here for the determination of VCDs of NO_2 is validated against experimentally derived composite profiles of NO_2 (aircraft + ground measurements) collected during BAQS-Met, and compared to spatially and temporally coincident VCDs of NO_2 determined from the satellite instruments OMI and SCIAMACHY. The aerosol optical depth values are compared to spatially relevant OMI, MODIS, AERONET, and $PM_{2.5}$ measurements. Case studies are presented to demonstrate the ability of MAX-DOAS to detect the complex transport of NO_2 in this region.

2 Experimental

2.1 BAQS-Met Ridgetown supersite

Measurements were acquired at the Ridgetown site (Fig. 1), during the BAQS-Met field study, 20 June–10 July 2007. Ridgetown is a rural community with a population of ~3500. The measurement site (42.45° N, 81.89° W), at an elevation of 202 m a.s.l., was located in an agricultural field at the north end of the University of Guelph (Ridgetown campus) away from the town center and direct anthropogenic influences. Surrounding sources (distance and direction) that can influence the site include a major highway, HWY 401 (4 km N), major refineries and chemical industry in Sarnia, ON (70 km NW), 2 major coal-fired power plants (65 km NW), Detroit/Windsor (100 km W), Cleveland, OH (100 km S) and the Golden Horseshoe (Toronto/Hamilton) urban area (200 km NE). Numerous urban areas and coal-fired power plants are also located in the Ohio valley region (100–500 km, S–SW). The site was 10 km from the north shoreline of Lake Erie.

2.2 The MAX-DOAS instrument and retrieval

The MAX-DOAS instrument used to measure scattered sunlight included a 1 m focal length Newtonian telescope (Sky Watcher, f/5) with a 20 cm primary mirror and a field of view of 0.06°. A stepper motor controlled the elevation angle (α), over the range from 0° (horizon) to 90° (zenith) with an error of ±0.2°. A fiber optic coupler in the telescope eyepiece focuses light into the fiber optic (2 m, 1000 µm diameter UV enhanced) that transfers light to a CCD spectrometer (Ocean Optics USB 2000^+, 323–471 nm, grating #7, 2400 lines mm^{-1}, 50 µm slit, UV4 upgrade, L4 lens), with 0.5 nm resolution. The spectrometer was housed in a Peltier cooling thermoelectric unit (Resonance Inc.) to achieve a stable temperature of 15 ± 0.2 °C. The spectrometer data was transferred to a PC via USB connection, while a custom LabVIEW program automated the measurement sequence including light level determination, integration times, collection and storage of averaged spectra, and movement of the telescope elevation angle by stepper motor prior to the next measurement. Every measurement began with an automatic determination of light level. This information was used to adjust the integration time of the measurement, ensuring that all measurements had an approximately equal level of signal. One complete cycle lasting approximately 30 min, consisted of a series of measurements with the following elevation angles (α): 90°, 30°, 10°, 6°, 4°, 2°. Each measurement typically consisted of 2000 averages with integration times ranging between 30–2000 ms, depending on light conditions. With the rationale of studying the passage of lake breeze fronts at the site, the MAX-DOAS telescope was pointed in the SW direction ($\beta = 235°$), parallel to the shoreline of Lake Erie.

Each spectrum was corrected by subtracting an electronic offset and dark noise spectrum. These corrected spectra were analyzed using the well-known DOAS technique (Plane and Smith, 1995; Platt, 1994; Platt and Stutz, 2008). A wavelength calibration using WinDOAS (Fayt and Roozendael, 2011) was performed by fitting a noontime zenith spectrum ($\alpha = 90°$) taken on a clean day, henceforth called the Fraunhofer Reference Spectrum (FRS), to a high resolution solar spectrum (Kurucz et al., 1984)

that was convolved with the instrument's slit function. A Ring spectrum (Grainger and Ring, 1962) was calculated from the FRS with DOASIS (Kraus, 2006). The NO_2 and O_3 (223 K and 243 K) absorption cross sections (Bogumil et al., 2003; Vandaele et al., 1998) were convolved using WinDOAS to match the instrument's resolution, while the O_4 (Greenblatt et al., 1990) cross section was interpolated. To determine the NO_2 DSCD for each spectrum, a 3rd order polynomial, the logarithm of the FRS, the Ring spectrum, convolved NO_2, convolved O_3 (223 K) and an additive polynomial (stray light) were fit to the logarithm of the corrected measurement spectrum using WinDOAS in the fit range 410–435 nm. Figure 2 gives a sample fit for 20 June 2007, 09:46 EDT (Eastern Daylight Time = UTC-4). To determine the O_4 DSCD for each spectrum, a 4th order polynomial, the logarithm of the FRS, the Ring spectrum, interpolated O_4, convolved NO_2, convolved O_3 (223 K and 243 K) and an additive polynomial were fit to the logarithm of the corrected measurement spectrum in the fit range 355–385 nm.

2.3 The active DOAS instrument and retrieval

Measurements of ground-based NO_2 were made using an active DOAS instrument that has been described in detail previously (McLaren et al., 2010). A retro-reflector was located 1.06 km SW of the site ($\beta = 235°$) at an elevation of 6 m a.g.l., giving a total path length of 2.12 km and an average beam height of 3.5 m a.g.l. The return beam was focused onto a 200 µm diameter quartz fiber optic (Ocean Optics), which coupled the light into a miniature spectrometer (Ocean Optics USB2000, Grating #10, 295–635 nm, 1800 lines mm^{-1}, 2048 element CCD, 25 µm slit, UV2 upgrade, L2 lens, resolution ~0.5 nm). Spectra were acquired with integration times between 150–350 ms and 4000 averages, for a time resolution of 7–13 min. Mercury lamp spectra were collected periodically for wavelength calibration and for convolving molecular reference spectra to the slit function of the spectrometer. Each ambient spectrum was corrected for electronic offset and dark noise. All spectra were fit using DOASIS (Kraus, 2006) in the range of 422–450 nm. The NO_2 fit scenario included a Xe lamp reference spectrum, convolved spectra of NO_2 (Vandaele et al., 1998) and O_3 (223 K) (Bogumil et al., 2003),

and a 3rd order polynomial. The detection limit (3σ) for NO_2 was 1.1 ppb, determined by repetitive determination of a low concentration sample.

2.4 SCIAMACHY satellite measurements

The SCanning Imaging Absorption spectroMeter for Atmospheric CHartographY (SCIAMACHY) on board the European Space Agency's ENVIronmental SATellite (ENVISAT) (Bovensmann et al., 1999) measures Earthshine spectra from the UV to the NIR with a spectral resolution of 0.22–1.48 nm. It is operated in different viewing geometries, including nadir and limb. In nadir geometry (directed vertically down), the footprint of a single pixel is $\sim 30 \times 60\,km^2$. Global coverage of nadir measurements is achieved every 6 days. In standard operation mode, the measurement state alternates between limb geometry (directed horizontally, tangential to the Earth's surface), and nadir in such a way that limb measurements probe almost the same stratospheric air mass as subsequent nadir measurements.

From the Earthshine spectra measured by SCIAMACHY, total slant column densities of NO_2 are determined using the DOAS fitting technique (Platt and Stutz, 2008). For the NO_2 fit in the spectral range 431–460 nm, appropriately convolved absorption cross sections of O_3, NO_2, O_4, H_2O, H_2O (liquid), and CHOCHO, Ring spectra accounting for vibrational and rotational Raman scattering, and a 5th order polynomial are included (Beirle et al., 2010). In order to extract tropospheric column densities, the stratospheric fraction is estimated and subtracted. This was done using the Reference Sector Method (Beirle et al., 2010). Stratospheric column densities are estimated over the remote Pacific and the remaining tropospheric residuals are corrected for longitudinal variations using the limb measurements of SCIAMACHY. For the conversion of tropospheric SCDs into VCDs of NO_2 (VCD_{SCIA} values), tropospheric AMFs are calculated via the RTM McArtim (Deutschmann et al., 2011), assuming a fixed tropospheric profile with 80% of the tropospheric NO_2 within a constant boundary layer with a height of 1 km (Chen et al., 2009).

2.5 OMI satellite measurements

Onboard the Aura satellite, the Ozone Monitoring Instrument (OMI) is a nadir-viewing spectroradiometer that uses a 2-D CCD to simultaneously measure the Earthshine spectra in the UV-Vis range from 270–500 nm (Levelt et al., 2006). Specifically, OMI measures in three broad spectral regions (UV-1, UV-2, Vis) with a spectral resolution between 0.45 and 1.0 nm. It provides global coverage daily with a pixel size of $13 \times 24\,km^2$ at nadir increasing to $\sim 40 \times 160\,km^2$ at the two ends of the scan line.

The present study uses the NASA standard product (overpass version) of the VCD of NO_2 (VCD_{OMI}) obtained from the NASA Aura Validation Data Centre (AVDC) website (NASA, 2010b). From the Earthshine spectra measured by OMI, total slant column densities of NO_2 are determined using the DOAS fitting technique (Platt and Stutz, 2008). For the NO_2 fit in the spectral range 405–465 nm, appropriately convolved absorption cross sections of O_3 (Burrows et al., 1999), NO_2 (Vandaele et al., 1998), H_2O (Harder and Brault, 1997), a Ring spectrum (Chance and Spurr, 1997) accounting for vibrational and rotational Raman scattering, and a cubic polynomial are included. To convert these SCDs into VCD_{OMI} values, different types of AMFs were calculated using geographically gridded ($2.5^\circ \times 2.0^\circ$) annual mean NO_2 profiles (GEOS-CHEM was used for tropospheric, and the Goddard Chemical Transport model was used for stratospheric profiles Bucsela et al., 2006). Details of the algorithm used for the retrieval of the VCD_{OMI} may be found in (Boersma et al., 2001; Bucsela et al., 2006; Celarier et al., 2008; Wenig et al., 2008).

2.6 MODIS and OMI aerosol products

The MODerate resolution Imaging Spectroradiometer (MODIS) provides the aerosol optical depth over portions of the continents and over oceans, from two satellites (Terra, Aqua). Daily level 2 data products provide a spatial resolution of a 10×10 1-km pixel array (nadir). Two MODIS aerosol level 2 data products, collection 5, MOD04_L2 and MYD04_L2, from the Terra and Aqua satellites respectively, are available from the Level

1 and Atmospheric Archive and Distribution System (LAADS) website (NASA, 2010a). Only those data products that overlapped Ridgetown were used. All MODIS aerosol optical depth values were found at $\lambda = 550$ nm, and had a maximum sensitivity over land of $0.05 \pm 15\%$ (Levy et al., 2007). OMI Aerosol Optical Depth (τ) values were taken from the NASA AVDC (NASA, 2010b). The OMAERUV L2 product was selected ($\lambda = 388$ nm) for a satellite overpass of Ridgetown. Information on this OMI near-UV retrieval algorithm may be found in Torres et al. (1998).

2.7 AERONET aerosol products

AErosol RObotic NETwork (AERONET) aerosol optical depth (τ) values were taken from direct solar measurements using CIMEL sun photometers at two measurement sites (Kellogg, Michigan, USA 42.41° N, 85.37° W, 293 m a.s.l., and Egbert, Ontario, Canada 44.23° N, 79.75° W, 264 m a.s.l.) (NASA, 2010c). All τ values used have an uncertainty of ~0.01 to 0.02 ($\lambda = 340$ and 380 nm) and were AERONET Version 2.0, Level 2.0 – quality assured data, meaning they were pre- and post-field calibrated, automatically cloud cleared and manually inspected. Details regarding the AERONET network, and the procedures used to calculate aerosol optical depths may be found in (Dubovik and King, 2000; Holben et al., 1998, 2001).

2.8 Additional supporting measurements

The NO_2, SO_2, and $PM_{2.5}$ were measured at ground level using a chemiluminescence NO_x analyzer with Mo converter (Thermo Model 42C), trace level pulsed fluorescence SO_2 analyzer (Thermo Model 43C-TL), and Tapered Element Oscillating Microbalance (TEOM) ambient $PM_{2.5}$ monitor (R& P Model 1400B with sample equilibration system) respectively. These measurement devices were located in the Ontario Ministry of the Environment's mobile particulate laboratory at the Ridgetown site. Measurements of NO_2 and other meteorological measurements were also made on-board the NRC Twin Otter Aircraft that was dedicated to the BAQS-Met field campaign. The NO_2

measurements were performed with a chemiluminescence NO_x instrument (TECO 42S) retrofit with a photolytic converter, for measurement of "true" NO_2 (±15%), with a detection limit of 60 pptv (3σ, 1 min). Details on the aircraft campaign measurements are provided in Hayden et al. (2011).

3 Methodology for determining τ and NO_2 VCDs from MAX-DOAS

The result of the MAX-DOAS retrieval (Sect. 2.2) is the DSCD:

$$\mathrm{DSCD}_\alpha = \mathrm{SCD}_\alpha - \mathrm{SCD}_{90} \quad (1)$$

where SCD_α and SCD_{90} are the slant column densities of measurements with $\alpha < 90°$ and $\alpha = 90°$ respectively. The DSCD represents the difference in column amount of the absorber integrated along the light path through the atmosphere and the column amount of the absorber in the SCD_{90}. It depends on the trace gas amount, elevation angle (α), solar zenith angle (SZA), and relative azimuth angle (RAZI) between the sun and the direction the telescope is pointed (β).

The AMF is the average light path enhancement for solar light traveling through the atmosphere compared to a straight vertical path orthogonal to the ground (Perliski and Solomon, 1993; Solomon et al., 1987). It is defined as:

$$\mathrm{AMF} \equiv \frac{\mathrm{SCD}}{\mathrm{VCD}} \quad (2)$$

Similarly, the differential air mass factor (DAMF) is defined as:

$$\mathrm{DAMF} = \frac{\mathrm{DSCD}}{\mathrm{VCD}_{\mathrm{trop}}} \quad (3)$$

Since the DSCD contains only tropospheric trace gas absorptions, for the calculation of the DAMF, only the tropospheric profiles of the trace gases have to be taken into

account (Sinreich et al., 2005). Expanding and rearranging Eq. (3) gives:

$$\mathrm{VCD_{trop}} = \frac{\mathrm{DSCD}}{\mathrm{DAMF}} = \frac{\mathrm{SCD}_\alpha - \mathrm{SCD}_{90}}{\mathrm{AMF}_\alpha - \mathrm{AMF}_{90}} \quad (4)$$

Unfortunately the conversion from DSCD to VCD is not easy, because the accurate determination of the DAMF is often difficult.

3.1 The geometrical approximation

Using a simple geometrical consideration, the AMF for an absorbing gas may be approximated if the trace gas layer is located below the scattering altitude:

$$\mathrm{AMF_{GEO}} = \frac{1}{\sin\alpha} \quad (5)$$

Conveniently a DSCD measured at 30° then equals the geometric VCD:

$$\mathrm{VCD_{GEO}} = \frac{\mathrm{DSCD}}{\mathrm{DAMF_{GEO}}} = \frac{\mathrm{DSCD_{30}}}{\frac{1}{\sin(30°)} - \frac{1}{\sin(90°)}} = \frac{\mathrm{DSCD_{30}}}{2-1} = \mathrm{DSCD_{30}} \quad (6)$$

This geometrical approximation assumes that the stratospheric absorption is similar in the horizontal-viewing and zenith directions (essentially canceling each other out). If there is a large amount of aerosol present, and hence a high degree of Mie scattering, this approximation becomes inaccurate. In most cases a RTM must be employed to obtain an accurate AMF (Hendrick et al., 2006; Wagner et al., 2007). In general, this approximation would only hold under clear sky and low aerosol conditions. For this study, geometrically approximated VCDs were determined using NO_2 DSCDs at both 30° and 10°. If a pair of geometric VCDs at these elevation angles in the same measurement series agreed to within 15%, then the $\mathrm{VCD_{GEO}}$, as defined in Eq. (6), was retained. This criterion ensures that the geometrical approximation is valid, and eliminates measurement points greatly affected by horizontal inhomogeneites, aerosols, or clouds (Frieß et al., 2006; Brinksma et al., 2008).

3.2 Radiative transfer and inversion

In southwestern Ontario, conditions with low aerosol levels are infrequently encountered during the summer and the geometrical approximation often does not hold. Instead, a RTM was used to determine the AMFs (Hendrick et al., 2006; Wagner et al., 2007). McArtim is a backward model that calculates the photon flux at a certain location (latitude, longitude, altitude) in the atmosphere treating multiple scattering with full spherical geometry (Deutschmann et al., 2011). AMFs were calculated for O_4 and NO_2 from McArtim simulated radiances. Input parameters to McArtim include α, SZA, RAZI, altitude, pressure, temperature, surface albedo = 0.05, single scattering albedo (SSA) = 0.95, asymmetry parameter (g, under the Henyey-Greenstein approximation = 0.68), and parameters for the absorbing trace gases.

Wagner et al. (2004) introduced the concept of using the oxygen dimer (O_4) absorption to retrieve aerosol profiles (Frieß et al., 2006; Li et al., 2010; Wittrock et al., 2004). O_4 results from the bimolecular association of O_2:

$$\mathrm{O_2 + O_2 \rightleftharpoons O_4} \quad (R3)$$

and is temperature and pressure dependent with a scale height of approximately 4 km. An estimated O_4 VCD (expressed as the integrated quadratic O_2 concentration) may be calculated if temperature and pressure vertical profiles are known. This was done for the Ridgetown site using radiosonde data from White Lake, Michigan (UWYO, 2010). The estimated O_4 VCD was 1.28×10^{43} molecules^2 cm^{-5}. This value agrees with other calculated values using similar approaches at similar elevations: 1.30×10^{43} molecules^2 cm^{-5} (Wagner et al., 2009), 1.26×10^{43} molecules^2 cm^{-5} (Wagner et al., 2002). Since most O_4 is predominately in the lowest part of the troposphere, this is the region where O_4 DSCDs are most sensitive to changes in the light path due to varying levels of aerosols. The amount of aerosol present for a given day and location also has a very large effect on the DAMFs.

3.2.1 Aerosol optical depth (τ)

Aerosol optical depth, τ, is the attenuation of light due to aerosol extinction; where I_0 is the original intensity of light, I the intensity after traveling a distance x, and E the aerosol extinction coefficient:

$$\frac{I}{I_0} = e^{-\tau} = e^{-Ex} \tag{7}$$

Typically τ is defined for light traveling through a vertical column of the atmosphere from sea level to infinity (top of the troposphere), in which E is not constant with height. In order to model conditions with varying degrees of aerosol load, an integrated aerosol optical depth is defined as:

$$\tau = \int_{0\,\mathrm{km}}^{20\,\mathrm{km}} E(z)dz \tag{8}$$

where z is the height above the ground (km). In the modeling performed here, E was calculated according to the following equation, as developed in Li et al. (2010):

$$E = \frac{\tau_{\mathrm{RTM}}}{H_{\mathrm{aer}}} \tag{9}$$

where τ_{RTM} is the aerosol optical depth determined using the methodology outlined below, and H_{aer} the aerosol layer height, which is equivalent to the boundary layer if aerosols are 100% confined to the boundary layer (also see Zieger et al., 2011).

Figure 3 provides a complete scheme of the methodology used in this study. The approach used by Li et al. (2010) to determine aerosol optical depths was extended to obtain NO_2 VCDs on a routine basis. A comprehensive description, sensitivity analysis, and further validation is in preparation (Wagner et al., 2011). McArtim was used to calculate O_4 AMFs at a wavelength of 360 nm, for 50 000 photon paths. A comprehensive set of O_4 DAMFs was catalogued (as a function of input parameters), and used to construct an O_4 DAMF look up table (L_α). A MATLAB routine was used to minimize

the difference between O_4 DAMFS in L_α, as a function of τ and H_{aer}, and O_4 DAMFs found via the measured DSCDs and their corresponding O_4 VCDs (M_α):

$$\chi^2(\tau, H_{\mathrm{aer}}) = \sum_{\alpha=2^\circ}^{30^\circ} \left[\frac{M_\alpha - L_\alpha(\tau, H_{\mathrm{aer}})}{\sigma(M_\alpha)}\right]^2 \tag{10}$$

The results of the minimization yield O_4 DAMF, τ, and H_{aer} values that may be used to describe the aerosol conditions for each cloud-free measurement series.

3.2.2 NO_2 vertical column densities

In addition to the dependence on the aerosol profile, NO_2 DAMFs are also a function of the vertical concentration profile of NO_2. Under the assumption of a horizontally homogeneous trace gas distribution, the atmosphere may be divided vertically into several layers of height, h. Each "box" will have its own DAMF, as follows:

$$\mathrm{DAMF}_{\mathrm{box}_i} = \frac{\mathrm{dDSCD}}{\mathrm{dVCD}_i} \tag{11}$$

where dDSCD is the partial DSCD, and dVCD_i is the partial VCD for box_i. Total DAMFs, from 0 m a.g.l. to the top of the atmosphere (TOA) are:

$$\mathrm{DAMF}_{\mathrm{total}} = \frac{\sum_0^{\mathrm{TOA}} \mathrm{DAMF}_{\mathrm{box}_i} \cdot \mathrm{VCD}_i}{\sum_0^{\mathrm{TOA}} \mathrm{VCD}_i} \tag{12}$$

McArtim was used to calculate NO_2 $\mathrm{DAMF}_{\mathrm{box}}$ values at 413 nm (within the DOAS fit range) using 50 000 photons for NO_2. These $\mathrm{DAMF}_{\mathrm{box}}$ values were catalogued in a $\mathrm{DAMF}_{\mathrm{box}}$ look up table. A MATLAB routine selects the appropriate subset of $\mathrm{DAMF}_{\mathrm{box}}$ from the look up table, based on the aerosol scenario previously determined (Eq. 10). NO_2 $\mathrm{DSCD}_{\mathrm{meas}}$ ratios were prepared by taking individually measured SCD_x values ($\alpha \leq 30^\circ$) and subtracting them from the SCD_{90} for a given series, then dividing each

DSCD by the $DSCD_{10}$. These $DSCD_{meas}$ ratios were then compared to their corresponding NO_2 $DAMF_{total}$ ratios. The "best fit" between the $DSCD_{meas}$ ratios and the possible $DAMF_{total}$ ratios gives the NO_2 layer height, H_{gas}, and the NO_2 DAMF for a given measurement series as well as the NO_2 VCD_α values via the following equation:

$$VCD_\alpha = \frac{DSCD_{meas}}{DAMF_{total}} = \frac{SCD_{meas}(\alpha) - SCD_{meas}(90^\circ)}{AMF_{total}(H_{gas}, \alpha) - AMF_{total}(H_{gas}, 90^\circ)} \quad (13)$$

Average NO_2 VCDs (henceforth called VCD_{RTM}) were calculated for each series:

$$VCD_{RTM} = VCD_{avg} = \overline{VCD}_{(2^\circ,4^\circ,6^\circ,10^\circ,30^\circ)} \quad (14)$$

4 Results and discussion

4.1 Aerosol optical depth/aerosol extinction coefficient

Figure 4 displays the O_4 DSCD values at Ridgetown for the entire field campaign, under cloud-free conditions. The O_4 DSCDs typically increase with decreasing elevation angles, indicative of a tropospheric absorber, such as on 20, 22, 23, 29 June and 2 and 7 July. However, in several cases (parts of 25, 26, 27 June, and 4, 5, 9, and 10 July) there appears to be little dependence of the DSCDs on elevation angle. This phenomenon occurs when high levels of aerosol and/or clouds are present and thus the light path from the last scattering event to the detector becomes effectively equal, regardless of the elevation angle of the observation. As only cloud-free conditions are presented here, the effect is largely due to the presence of aerosols. As such, when qualitatively comparing aerosol levels, days such as 20 June appear to contain low aerosol extinction, while days such as 9 July, contain elevated aerosol extinction.

In order to assess conditions on a more quantitative level, the aerosol optical depth (τ_{RTM}) for each measurement series was determined at 360 nm as described in Sect. 3.2.1 (Fig. 5). The τ_{RTM} varied from 0.05 to 2.93, with a mean and a median value of 0.41 and 0.46 respectively. The average relative error of each τ_{RTM}

value was estimated at 26% (Wagner et al., 2011). The τ_{RTM} values were compared to those τ values found from satellite measurements (τ_{MODIS}: $\lambda = 550$ nm, τ_{OMI}: $\lambda = 388$ nm), and AERONET ground based measurements at Egbert and Kellogg (τ_{EGB}, τ_{KEL}, $\lambda_{avg} = 360$ nm for each location). Satellite measurements are only optimally available on a daily basis. The comparison was limited due to the different wavelengths used (particularly for τ_{MODIS}) and the fact that the satellites only provide 1 or 2 comparison points daily. Although the measurements are made at similar λ for the AERONET locations, they are relatively far from Ridgetown (Egbert ~320 km NE, Kellogg ~330 km W), yet Ridgetown is approximately central between the two locations. The above factors limit the ability to make direct comparisons of τ_{RTM} at Ridgetown, yet the values of τ_{RTM} do lie within the range of the other measurements, as might be expected during times when the high aerosol loading is associated with regional pollution events that affect eastern North America over large spatial distances. Such regionally polluted conditions were observed from 24–27 June and 8–10 July .

Spatially, it would be better to compare the τ_{RTM} values with aerosol levels measured directly at Ridgetown. Although another measure of τ is not available at the site, $PM_{2.5}$ mass was measured. When the $PM_{2.5}$ was compared to the corresponding τ_{RTM} values, a low level of correlation was found ($R^2 = 0.068$). This is not surprising since $PM_{2.5}$ is a ground point-source measurement of particulate mass, while τ_{RTM} represents an integrated column quantity of aerosol extinction. A more appropriate comparison of the aerosol properties may be done by examining the aerosol extinction coefficient, E.

Figure 6a shows the time series comparing the aerosol extinction coefficient calculated via Eq. (9) and the $PM_{2.5}$ measured at Ridgetown. A correlation plot for these two related properties is shown in Fig. 6b using data from the entire study. Both panels show that there is a high degree of correlation between aerosol extinction and $PM_{2.5}$ ($R^2 = 0.75$) (also see Zieger et al., 2011). This improved correlation implies that MAX-DOAS observations are sensitive to the total column amount of aerosol, in comparison to the $PM_{2.5}$ measurement that is sensitive to the concentration of aerosol. It also implies that temporal variations in the aerosol layer height, H_{aer}, are likely significant at

Ridgetown.

Recent studies have compared local PM_{10} and $PM_{2.5}$ measurements to τ values determined from MODIS (Chu et al., 2003; Engel-Cox et al., 2004, 2006; Gupta and Christopher, 2008; Kacenelenbogen et al., 2006; Pelletier et al., 2007; Schaap et al., 2009; Wang and Christopher, 2003). The extent of correlation they found between τ_{550} (MODIS) and $PM_{2.5}$ varied, with R^2 values ranging from 0.27 to 0.60. This range is not entirely surprising as variations in local meteorology, differing aerosol composition, and the distribution of the aerosol layer(s) may all play roles in this relationship. In particular if aerosols are concentrated in the boundary layer, and the boundary layer is highly variable, a poor relationship between τ and $PM_{2.5}$ would be expected. If the boundary layer height is known, this correlation may be greatly improved through calculation of E. For example, Koelemeijer et al. (2006) found that there was a better correlation ($R^2 = 0.59$) between $PM_{2.5}$ measurements and the modified aerosol extinction from MODIS, E^*:

$$E^* = \frac{\tau}{\mathrm{BL} \cdot f(\mathrm{RH})} \tag{15}$$

with BL being the boundary layer height, and f(RH) a factor that takes into account the hygroscopic growth of aerosols, as opposed to directly comparing hourly $PM_{2.5}$ and τ ($R^2 = 0.38$). Their result, like ours, implied that most of the aerosol was found within the boundary layer, whose height is variable, preventing an easy direct measurement of aerosol mass through satellite derived quantities.

Further studies have determined aerosol extinction coefficients and aerosol optical depths from MAX-DOAS O_4 measurements and radiative transfer modeling, and compared them to PM_{10}, LIDAR calculated extinction coefficients, and aerosol optical depths from sky radiometers. Irie et al. (2008) compared extinction coefficients from MAX-DOAS-RTM inversions run at 476 nm with LIDAR calculated extinction coefficients (slope = 1.01, $R^2 = 0.85$) and compared τ values found from these MAX-DOAS-RTM inversions with τ values from a sky radiometer. Both comparisons agreed to within 30% for values determined from ground level to a height of 1 km. Lee et al.

(2009) compared extinction coefficients found from a MAX-DOAS-RTM inversion run at 356 nm to LIDAR calculated extinction coefficients ($R^2 = 0.70$), and they agreed to within 50%, while a comparison between MAX-DOAS-RTM derived extinction coefficients and PM_{10} also showed a relatively good correlation. Our results are consistent with these studies.

4.2 Validation of VCD_{RTM} against vertical measurements of NO_2

In order to validate our method for deriving NO_2 VCDs using MAX-DOAS and RT calculations, we derived comparative VCDs of NO_2 from a composite of ground-based and aircraft-based NO_2 measurements in the vicinity of Ridgetown during the same time frame as the MAX-DOAS measurements. The composite profiles included ground-based NO_2 measurements at Ridgetown via active DOAS, vertical measurements of NO_2 when the aircraft was in the vicinity of Ridgetown, and suitable estimates of NO_2 in the free troposphere above the maximum height of the aircraft. Suitable temporal and spatial overlapping data were found for one day, 26 June 2007. Four composite profiles of NO_2 were derived for this day, two in the morning when the boundary layer height was still low, and two in the late afternoon, when the boundary layer had maximized. The morning profiles were split into three discrete sections. Within the boundary layer (Sect. I), the NO_2 mixing ratio was assumed to be homogeneous and equivalent to the NO_2 measured at ground level by DOAS. Boundary layer heights for this time period were determined through a combination of LIDAR, vertical temperature profiles measured by tethersonde at the site, and by aircraft in the vicinity of the site. For Sect. II, the portion of the column from the top of the boundary layer to the maximum height of the aircraft, NO_2 measured onboard the aircraft was used when the aircraft was within a suitable criteria distance of the Ridgetown site. In general, the degree of spatial homogeneity in NO_2 increases with height, in the absence of elevated sources, and our criteria for inclusion of data in the composite profile reflected this. From the top of the boundary layer to 800 m a.g.l., only aircraft data collected within 30 km of the site was included, while from ~800 m to 1600 m a.g.l. aircraft data within 80 km of the site was

included (Fig. 7a). The assumption here is that above the boundary layer in the morning, the NO_2 mixing ratio in the residual layer is regionally homogeneous. For Sect. II, NO_2 number densities were calculated as a function of height accounting for the non-linearity of pressure and temperature, then fit to an exponential function, and integrated over the appropriate range to yield the NO_2 column density. For Section III, the portion of the column above the top of the aircraft measurements (free troposphere), a constant NO_2 mixing ratio of 50 ppt was assumed (Blond et al., 2007).

For afternoon profiles, the boundary layer was much higher and the assumption of a homogeneous layer of NO_2 was found to be invalid on this day. Mixing ratios of NO_2, measured when the aircraft penetrated into the boundary layer (~315 m a.g.l.) over land close to Ridgetown, were much lower than values measured at ground level. The boundary layer at this time was 797 ± 45 m a.g.l., determined by potential temperature profiles measured by the aircraft. For this reason, the PM profiles were split into just two sections, with Sects. I and II combined in this case. Sections (I + II) consisted of the portion of the column from ground level to the top of the aircraft measurements. Our criteria for inclusion of aircraft data in the profile was that the aircraft had to be within 30 km of the site over land for the boundary layer, within 50 km of the site for heights from the top of the boundary layer to 1400 m a.g.l., and within 140 km of the site for heights between 1400 and 2980 m a.g.l. (Fig. 7c). To determine the total column density of this section, an exponential was fit to all NO_2 data from ground level to the top of the available aircraft measurements. This exponential fit was then integrated to obtain the total NO_2 column density for this section. A sensitivity calculation is included later on to explore the uncertainty in this approach. Section III was again assumed to have a constant NO_2 mixing ratio of 50 ppt.

The vertical column densities of NO_2 calculated from these profiles are henceforth called composite VCDs (VCD_{COMP}):

$$VCD_{COMP} = \int_0^{BL} n^{I}_{NO_2} dz + \int_{BL}^{TOAc} n^{II}_{NO_2} dz + \int_{TOAc}^{10\,km} n^{III}_{NO_2} dz \quad (16)$$

where n_{NO_2} is the number density of NO_2 for Sects. I, II, III, and TOAc represents

the top of available aircraft measurements. Figure 7a (08:32–11:07 EDT) and Fig. 7c (16:07–18:21 EDT) show the flight path used for each flight. In each figure, the NO_2 mixing ratio is displayed as a function of time and location. The exact position of the aircraft for every 10-minute interval of flying time is also marked. Figure 7b and 7d show the altitude profiles for these flights with respect to time of day, and include ascending, descending, and stable height time periods. The closest available NO_2 mixing ratios for each given height have been selected based on both time and location considerations, as discussed previously. Figure 8 displays two sample profiles. Error bars in the *y* dimension represent uncertainties in the boundary layer heights (AM period only), while error bars in the *x* dimension represent uncertainties in the NO_2 mixing ratios.

Four VCD_{COMP} values were determined for the AM and PM flights on this day, to be compared to four VCD_{RTM} values coincident in time (Table 1). The uncertainties in the VCD_{COMP} arise from several sources. For Sect. I (AM), the contributing factors were the uncertainty in the boundary layer height and the uncertainty in the DOAS NO_2 concentration. These two uncertainties were propagated to give the total uncertainty for Sect. I. For each AM measurement the boundary layer was determined from LIDAR with uncertainty, and verified using temperature profiles from tethersonde/aircraft measurements. For Sect. II, the uncertainty in the exponential fit of NO_2 mixing ratio vs. height was primary. For Sect. III the uncertainty in the assumed NO_2 mixing ratio (50 ppt) was assumed to be ±100%. For Sects. (I + II, PM), the uncertainty in the exponential fit was primary, and for Sect. III (PM), the uncertainty in the NO_2 mixing ratio was again assumed to be ±100%. Uncertainties due to spatial and temporal differences between the aircraft measurements and the MAX-DOAS column also exist but were not considered. The uncertainty of VCD_{RTM} was estimated based on the comparison of VCD_{COMP} and VCD_{RTM} in Table 1. The relative RMSE of the measurements was 25%. This is our estimated relative uncertainty in the determination of VCD_{RTM}.

The mean value of the VCD_{COMP} values in Table 1 was $3.54 \pm 0.59 \times 10^{15}$ molec cm^{-2}, which is reasonable for a rural region (Heland et al., 2002; Irie et al., 2009; Ladstätter-Weißenmayer et al., 2003). The mean value of the VCD_{RTM} values was $4.03 \pm 0.71 \times$

10^{15} molec cm^{-2}. The ratio of $VCD_{RTM}/VCD_{COMP} = 1.14 \pm 0.27$, while the regression of VCD_{RTM} vs. VCD_{COMP} indicates a slope of 1.16 ± 0.12 (1σ) that is not statistically different from 1.0 at the 95% confidence level. The regression was forced to zero because the intercept in a two parameter linear regression did not show an intercept that was statistically different from zero. The mean bias in the VCD_{RTM} values compared to the VCD_{COMP} values is $+0.49 \times 10^{15}$ molec cm^{-2}, again not statistically different from zero. Although we have only compared a limited number of points, the comparison above serves as a preliminary validation of the method outlined in this paper for the determination of VCDs. There is no evidence of a statistically significant bias in the determination of VCD using this method at the moderate NO_2 column levels that existed during the comparison.

4.3 Comparison between VCD_{RTM} and satellite VCDs of NO_2

Figure 9 displays all tropospheric VCDs of NO_2 for the Ridgetown site throughout the study. The VCD_{RTM}, VCD_{GEO}, and VCD_{COMP} (26 June) are shown, along with the satellite-derived measures VCD_{OMI} and VCD_{SCIA}. Only 9 VCD_{SCIA} measurements were available during the study period due to the limited temporal sampling of the ENVISAT satellite. There were 31 measurements from the OMI instrument on the Aura satellite as it provides daily global coverage with successive orbits separated by 100 min providing one or two measurements per day at a specified location. To facilitate comparisons between VCD_{RTM} and $VCD_{satellite}$, measurements were paired only when the two measurements were made within one hour of each other. Only one comparison pair was available for SCIAMACHY while 8 comparisons were available for the OMI instrument. The statistical comparison is provided in Table 2, where all VCDs are compared to VCD_{RTM}. The comparison indicates that the VCDs derived by satellite were higher than those of the VCD_{RTM}. Presuming a proportionate error, the two satellites determinations are about 50% higher than VCD_{RTM}, but only statistically so for the OMI instrument. The proportionate error for OMI was determined in two ways:

(i) the ratio of the averages, VCD_{OMI}/VCD_{RTM}, and (ii) the slope of the regression of VCD_{OMI} vs. VCD_{RTM}, with the y-intercept forced to zero (intercept was equal to zero within error). If one presumes a constant bias in the satellite measurements, the absolute errors dictated by the mean error or the root mean square error (RMSE), falling in the range of $+0.5 - 1.3 \times 10^{15}$ molec cm^{-2} would be more appropriate. Our results do not provide sufficient statistical evidence of whether the satellite error is proportionate or absolute.

Earlier studies (Brinksma et al., 2008; Celarier et al., 2008; Chen et al., 2009; Irie et al., 2009) found various satellite-derived NO_2 VCDs to be substantially lower than MAX-DOAS derived NO_2 VCDs. It should be noted that in those studies the MAX-DOAS VCDs were geometrically approximated (similar to VCD_{GEO}), and the distinction from a full MAX-DOAS with radiative transfer derived VCD (VCD_{RTM}) should be taken into account in all these studies. Our observation of satellite VCDs with a positive bias compared to VCD_{RTM} and VCD_{COMP} is in contrast to the earlier studies. One possible explanation for this is that previous comparisons have frequently focused on urban and suburban areas where average NO_2 VCDs were significantly higher. For example, the VCD of NO_2 ranged from $0.5 - 5 \times 10^{16}$ molec cm^{-2} during DANDELIONS at Cabauw, Netherlands (Brinksma et al., 2008; Celarier et al., 2008) with a median of $\sim 1.5 \times 10^{16}$ molec cm^{-2}, whereas the VCD range in the current study is $0.01 - 1.25 \times 10^{16}$ molec cm^{-2} with a median of 2.00×10^{15} molec cm^{-2}. In that study, the MAX-DOAS instruments measured very high NO_2 VCDs in a polluted region, which could not be completely captured by the satellite, due to the regional averaging implicit with a large pixel size. Under such conditions, the satellite will measure lower values than the more localized in situ measurement. The opposite would be true in this study. Being situated in a rural region, the local measurements of NO_2 made by MAX-DOAS and the aircraft are relatively low. In contrast, the large pixel area coverage of the satellite instruments (OMI – 13×24 km^2, SCIAMACHY – 30×60 km^2) will be higher than the local measurement when the pixel is impacted by surrounding urban areas, such as may occur when prevailing westerly winds carry pollutants from Windsor-Detroit

towards Ridgetown. If a significant amount of a given pixel lies within a position west of Ridgetown, it may be detecting NO_2 from this urban outflow, and thus overestimate the actual NO_2 present at the site (see Fig. 10). Additionally, the satellite retrievals used here do not consider aerosol conditions or temporal changes in the NO_2 profile in their fitting routines. Uncertainties in these parameters could lead to uncertainties in the overall satellite-derived VCD, and with low levels of NO_2, this may lead to large relative uncertainties in these VCDs.

Also included in Table 2 is a statistical comparison of VCD_{GEO} to VCD_{RTM}, where the conservative selection criteria for inclusion was fulfilled, namely that the values of geometrically approximated VCDs for elevation angles of 10° and 30° in the same measurement series agreed to within 15%, similar to that used by others (Frieß et al., 2006; Brinksma et al., 2008). This criterion was fulfilled for 10 data pairs, as seen in the table. The comparison indicates that VCD_{GEO} is lower than VCD_{RTM} by 8–12%, presuming a proportional error, or with a mean error of -0.2×10^{15} molec cm^{-2}, presuming an absolute error. Since both of these VCDs are derived either partly or entirely from the same set of MAX-DOAS measurements, they have nearly identical measurement times, and compared pairs show a high correlation between VCD_{GEO} and VCD_{RTM} ($R^2 = 0.97$).

The average NO_2 VCD retrieved from OMI measurements during the study period (20 June–10 July 2007) for the BAQS-Met study domain is mapped on a $0.002^\circ \times 0.002^\circ$ grid, as described in Wenig et al. (2008), in Fig. 10. The highest VCDs are seen over the metropolitan area of Detroit/Windsor with average VCDs up to $\sim 1 \times 10^{16}$ molec cm^{-2}. Other areas with enhanced NO_2 columns include the cities of Toledo, Sarnia, and Cleveland. The waterways between Lake Huron and Lake Erie, one of the busiest waterways in the world, (St. Clair River and Detroit River) are also hot spots for enhanced columns of NO_2, and likely indicative of the heavy ship traffic and associated industrial activities supported by the presence of the waterway transport. Also visible from the satellite are enhanced NO_2 columns extending well out into the lakes at the ends of these waterways; Lake Erie (south of Detroit) and Lake Huron

(north of Sarnia) which are likely indicative of the emissions from underway vessels, anchored vessels awaiting entry into the waterways and recreational boating activities. Considering just the NO_2 VCDs over Lake Erie, the western region of the Lake appears to be the most polluted. In contrast, the measurement site at Ridgetown can be seen to be in a relatively rural area with a study average NO_2 VCD of $\sim 2-3 \times 10^{15}$ molec cm^{-2}. The lowest VCDs in the domain are seen over Lake Erie south of London and in regions surrounding London to the north and west.

4.4 Comparison between VCDs and ground level concentrations of NO_2

To examine the relationship between NO_2 vertical columns and NO_2 concentrations at ground level, average NO_2 concentrations were calculated for the time periods of all VCD_{RTM} determinations. In this analysis and in the case studies to follow, we have used the NO_2 determined from the chemiluminescence instrument (Sect. 2.8) due to the continuous and higher temporal resolution of data available from this instrument compared to the active DOAS instrument. It is well known that the "NO_2" reported for these instruments may be biased high since they may contain some contribution from NO_Z species ($NO_Z = NO_Y - NO_x$) due to reduction of NO_Z by the Mo convertor. However, for most of the periods of discussion to follow, we generally found good agreement between the NO_2 reported by the chemiluminescence and active DOAS instrument, apart from some early morning periods when we suspect that HONO and HNO_3 accumulated overnight may have contributed to the signal. Figure 11 shows three polar class scatter plots using the various NO_2 measures; where the NO_2 VCD_{RTM}, NO_2 number density (n_{NO_2}), and the ratio VCD_{RTM}/n_{NO_2} are plotted on the radial axis respectively, as a function of the average wind direction and the time of day, color-coded into 4 binned daytime periods. The temporal behavior of the NO_2 measures within each time bin are also tabulated in Table 3, irrespective of wind direction.

Three dominant factors can contribute to the daytime temporal trends in NO_2 observed at the site: (i) temporal changes in emission rates of local NO_x sources, (ii) changes in dilution effects of boundary layer NO_2 brought about by changes in

the boundary layer height, and (iii) changes in the Leighton ratio, $[NO_2]/[NO]$, brought about by changes in the photolysis rate of NO_2. The ground-based NO_2 concentrations show a clear dependence on the time of day, both in Fig. 11 and Table 3. The highest concentrations are seen in the early morning decreasing by a factor of ~3 by the afternoon. As this rural site is not impacted greatly by direct sources of NO_x, the decrease in NO_2 from early morning to afternoon is likely indicative of a combination of increased dilution in a growing boundary layer, as well as increased photoylsis of NO_2. The photolysis of NO_2 would give highest losses around solar noon (13:31 EDT at this site), and a corresponding minimum in the middle of the day. The lack of a significant minimum in the central bins of n_{NO_2} in Table 3 indicates that increased dilution in a growing boundary layer is the dominant factor that contributes to the temporal pattern seen for the NO_2 concentration. Conversely, the VCD_{RTM} shows less dependence on the time of day (Table 3 and Fig. 11), compared to the NO_2 concentration, and the temporal trend contains a minimum in the middle of the day. This is to be expected, as the column density of a pollutant in the boundary layer should be independent of dilution effects resulting from changes in the boundary layer height. The minimum VCD (1.5×10^{15} molec cm^{-2}) is observed in the bin that contains solar noon (Table 3) when NO_2 photolysis would be at its highest rate, while the highest VCD averages ($2.4\&2.7 \times 10^{15}$ molec cm^{-2}) were found in the early morning and early evening periods, when the NO_2 photolysis rate is significantly less than solar noon. These observations indicate that the photolysis of NO_2 and consequent lowering of the NO_2/NO ratio likely play a more dominant role in the temporal behavior of the NO_2 VCD.

To examine the differences between NO_2 vertical columns and NO_2 concentrations measured at ground level, the following ratio was calculated:

$$\text{Ratio} = \frac{\text{VCD}_{\text{RTM}}}{n_{\text{NO}_2}} = \text{BL}_{\text{eff}} \quad (17)$$

whereby the VCD_{RTM} and n_{NO_2} for identical time ranges were compared. In general, one would expect the NO_2 vertical column density and NO_2 concentration at ground

level to be correlated with one another. If NO_2 is well mixed within a homogeneous boundary layer, and the vertical column is dominated by NO_2 within the boundary layer, then this ratio will be approximately equal to the boundary layer height. However, as we have already seen (Sect. 4.2), the boundary layer is not always well mixed, and free tropospheric NO_2 can also contribute to the vertical column of NO_2, creating a deviation of the ratio from the true boundary layer height. For these reasons, we call this ratio the effective boundary layer height, BL_{eff}. A value of BL_{eff} higher than the actual boundary layer height would be observed under the following conditions: (i) an elevated plume of NO_2 exists above the surface site or (ii) the column of NO_2 in the free troposphere is a significant fraction of the total tropospheric column (e.g. likely observed under conditions when the boundary layer is relatively unpolluted). Conversely, values of BL_{eff} lower than the actual boundary layer would be observed when surface sources of NO_2 are not well mixed in the boundary layer, which could occur under conditions of relative atmospheric stability. In addition to these deviations of BL_{eff}, we also expect that the temporal pattern of BL_{eff} will generally follow the temporal pattern of the real boundary layer height.

The values of BL_{eff} observed during this study ranged from 12 m (observed in early morning) to 2.54 km (observed in late afternoon). In general the BL_{eff} increased from early morning to the end of the day (Table 3, Fig. 11), although the average values observed in the early afternoon (~200 m) are less that one would expect for continental boundary layer heights in midsummer in this region. This likely indicates that NO_2 is not homogeneously mixed in the boundary layer, as we directly observed by the aircraft measurements on 26 June (Sect. 4.2). Instructive here is to identify cases where the VCD measured by MAX-DOAS shows something different than what is measured by the more conventional surface-based point source measurement of NO_2. These cases would be indicated by the highest and lowest values of BL_{eff}. The periods of low BL_{eff} are somewhat trivial and are all isolated to early morning events, when a nocturnal inversion is still intact. During such periods, the NO_2 accumulated throughout the night from regional surface sources are trapped in the low inversion creating relatively high

concentrations of NO_2 but only low or moderate tropospheric VCDs. More interesting are periods with high levels of BL_{eff}, during which a ground-based measurement of NO_2 concentration would underestimate the total amount of NO_2 in the troposphere and transport of NO_2 into the region, with subsequent impacts on regional air quality. In Fig. 11, four such cases are identified as a function of the wind direction measured at ground level. The highest values of BL_{eff} occurred on 30 June, 2, 6 and 9 July 2007.

On 30 June (between 12:00–12:40 EDT), the highest value of VCD_{RTM} determined in the study was recorded (1.25×10^{16} molec cm^{-2}) and the BL_{eff} rose to 998 m. During this case, an elevated plume of NO_2 impacted the site from the NW that we attribute to industrial point sources in Sarnia. This case is discussed in further detail in the next section. On 2 July (between 15:00–18:00 EDT), on an otherwise cool, clear and clean day, the VCD_{RTM} increased to 5×10^{15} molec cm^{-2} and BL_{eff} = 991 m with virtually no increase in the ground level concentration of NO_2. We attribute this case to impact by elevated forest fire plumes, originating in northern Ontario that moved southward, while the ground level at Ridgetown experienced a clean lake breeze inflow from the southeast. On 6 July, the BL_{eff} had a maximum of 1.08 km early in the evening (17:00–19:00 EDT). Winds during this time were from the N–NW and the presence of elevated SO_2 indicates that the site was impacted by a mixture of industrial emissions from Sarnia, and possibly marine vessel emissions from ships on Lake Huron. The high boundary layer height would be typical of a lake breeze layer thermally modified after traveling 70 km inland (Sills et al., 2011). On 9 July late in the afternoon, the highest values of BL_{eff} (up to 2.5 km) were seen. This case was characterized by strong winds from the SW that is characteristic for southern Ontario, evidence for strong convection and extremely high pollution levels, a classic case of a pollution episode with long-range transport of pollutants from the SW. This case will also be discussed in more detail in the next section.

4.4.1 Case studies

Figure 12 summarizes measurements made on 30 June 2007 at Ridgetown. The synoptic flow was gentle and from the northwest in the morning period. Relatively high levels of ground level NO_2 (8–12 ppb) but low levels of SO_2 were seen in the morning period 08:00–10:00 EDT. At the same time, the NO_2 VCD_{RTM} was quite low ($<1 \times 10^{15}$ molec cm^{-2}), and BL_{eff} was $\leq$150 m, indicating a shallow inversion layer. Ground level NO_2 mixing ratios decreased rapidly due to the breakup on the nocturnal inversion at about 09:30 EDT and leveled off for the remainder of the morning at $\sim$2 ppb. The characteristic feature on this day was a pollution plume of $\sim$1 h duration that impacted the site between 12:00–13:00 EDT. During this short interval, daily maxima were observed for DSCDs ($\alpha = 2^\circ, 4^\circ, 6^\circ, 10^\circ$), VCD_{RTM}, τ_{RTM}, $PM_{2.5}$, SO_2, BL_{eff} (Fig. 12), and O_3 (52 ppb, not shown). The maximum of the pollution plume coincided with the arrival of a lake breeze front from Lake Huron to the north. Evidence for this was an increase in the relative humidity, a slight drop in temperature, in addition to results from an observational analysis of all lake breeze fronts and their temporal movement in the study region provided by Sills et al. (2011). The results from the MAX-DOAS measurements are particularly informative at this time. In particular, while the DSCDs of NO_2 increased at all elevation angles, the DSCD with $\alpha = 4^\circ$, $DSCD_4$, was higher than the $DSCD_2$, an unusual situation that strongly suggested that the polluted layer was elevated from the surface, or had higher concentrations above the surface than at ground level (Hönninger et al., 2004). This result can be contrasted to the result early in the morning when the nocturnal boundary layer was still intact. During that early morning period, we observed the typical situation in which $DSCD_2 > DSCD_4 > DSCD_6 > DSCD_{10} > DSCD_{30}$, commonly seen when a polluted layer exists at the surface, where larger DSCDs are observed at lower elevation angles due to the larger effective path length of scattered light through the polluted layer (Hönninger et al., 2004). Other evidence that the pollution plume was elevated was the rapid increase in the value of BL_{eff}. Despite the presence of an elevated plume,

increases in SO_2, NO_2, and NO_x were still seen at ground level during this time period of the plume, which coincided with the arrival of the lake breeze front. This suggests that the elevated plume was mixed partially to the surface (but not homogeneously) through a process known as fumigation, where smokestack effluent brought inland in stable stratified marine air is mixed to the surface when it intersects the convective mixed layer at the lake breeze front (Lyons and Cole, 1973; Sills et al., 2011).

Wind Directions on 30 June 2007 were N–NW (Fig. 12) and the pollutant plume between 12:00–13:00 EDT may be traced back to the region of Sarnia, Ontario ~70 km away, using back trajectory analysis (Fig. 13). Many anthropogenic sources with elevated stack emissions are located close to the Lake Huron shoreline close to Sarnia, including petrochemical refineries, other chemical industries, and a major coal fired electric generation facility in Lambton, Ontario. The excess SO_2/NO_x ratio (mole mole^{-1}) in the pollution plume at ground level during the pollution event was calculated to be 2.21 ± 0.08 mole mole^{-1}. This can be compared to emissions from the largest point sources within a 5 km radius of Sarnia that contain stacks. According to the National Pollutant Release Inventory (EC, 2011), the total emissions of SO_2 and NO_x from the top 10 point sources in Sarnia are 23.9 ktonnes yr^{-1} and 5.82 ktonnes yr^{-1} respectively, with a SO_2/NO_x ratio of 2.95 mole mole^{-1}, dominated by refinery emissions. The corresponding emissions of SO_2 and NO_x from the stack of the Lambton coal-fired electric utility (~16 km south of the major refineries in Sarnia) are 6.19 ktonnes yr^{-1} and 3.96 ktonnes yr^{-1}, with a SO_2/NO_x ratio of 1.10 mole mole^{-1}. Although we cannot identify a single source from this, the evidence suggests that the plume impacting the site during this period was from either one or several elevated fuel combustion sources that fumigated to the surface as the lake breeze front passed Ridgetown. After this time, the winds at the site continued to shift towards a more northerly direction and the site experienced a clean lake breeze from Lake Huron for the rest of the afternoon, devoid of surface or elevated pollution sources of NO_2. While evidence points to the fact that the plume was elevated, an explanation is still required for the large increase in the VCD and simultaneous arrival with the lake breeze front. A lake breeze front is known

to be a narrow convergence zone with enhanced lift that can transport pollutants upward. The front can also result in a region of spatial stagnation, with respect to the inflow layer, if the speed of the front moves slower than the inflow layer. The dynamics of both lift, and recirculation that exist at the front (Lyons and Cole, 1973; Sills et al., 2011) can thus result in a concentration of pollutants at the front. Our result presents evidence (perhaps for the first time) that these dynamics can lead to an overall increase in not only the concentration of pollutants, but also the vertical column of pollutants at the front as well. This is the first demonstration of such an effect using MAX-DOAS, to the best of our knowledge.

Figure 14 summarizes measurements made on 2 July 2007. The area was under the influence of a regional high pressure system on this day with light winds, sunshine, cool temperatures (< 21 °C) and "classic" lake breeze conditions (Sills et al., 2011). Ground level pollution (SO_2, NO_2, $PM_{2.5}$, O_3) was low throughout most of the day, as was O_3 (<35 ppb, not shown). The MAX-DOAS measurements indicated a clean troposphere with VCDs $< 2 \times 10^{15}$ molec cm^{-2} and $BL_{eff} < 200$ m prior to 15:00 EDT, indicating either a shallow or inhomogeneously mixed boundary layer with NO_2 confined to the surface. By late morning and throughout the afternoon, the site was experiencing a moderate lake breeze from the S–SE (Lake Erie) although satellite imagery indicates that upper air movement was from the W–NW. After 15:00 EDT, the VCDs of NO_2 showed an appreciable increase from $\sim 5 \times 10^{14}$ molec cm^{-2} up to 5×10^{15} molec cm^{-2}, while the BL_{eff} increased from less than 100 m to greater than 1 km. A close examination showed that the ground level mixing ratio of NO_2 remained unchanged at ~2 ppb throughout this period, indicating that the increase in vertical column of NO_2 was not due to a surface source of NO_2. Unlike the elevated plume seen on 30 June, in this case the DSCDs at lower elevation angles ($DSCD_2$, $DSCD_4$) did not show any appreciable increase. Further examination indicates that the increase in the VCD is being largely driven by increase in $DSCD_{30}$. In a qualitative sense, this indicates that the elevated NO_2 must be at very high elevation from the surface, much higher than seen on 30 June. Indeed, elevated forest fire plumes, visible as brown streaks high in the sky, and originating

from northern Canada (Saskatchewan) were reported this day in southern Ontario, and were clearly visible in the sky, moving south at high altitude, likely in the upper free troposphere. Although the aerosol optical depth was higher in the morning (τ_{RTM} = 0.4), likely due to continental aerosol pollution from the vicinity of Toronto (NE), τ_{RTM} increased marginally during the smoke plume event while $PM_{2.5}$ was unchanged or decreased slightly, an indication that a small amount of aerosol was likely associated with the biomass plume. Thus, this case study illustrates a situation where transport of pollution through the region at high altitude was detected by MAX-DOAS, but would be virtually undetected via ground level measurements.

Figure 15 summarizes measurements made on 9 July 2007. This day was characterized by warm temperatures (33 °C maximum), hazy conditions with strong W–SW synoptic flow, high deformation lake breezes around the lakes, and strong convective initiation (Sills et al., 2011). High pressure existed south east of the Great Lakes, a typical situation for the transport of ozone and aerosol precursors into southern Ontario from the SW (MOE, 2011). Indeed, aerosols were abundant with $PM_{2.5}$ levels in the range of 10–50 $\mu g\,m^{-3}$, and $\tau_{RTM} \sim 1.0 \pm 0.2$ in late afternoon, apart from a single value of 2.8 at 17:00 EDT. Ozone also recorded a maximum of 87 ppb, a few minutes prior to the passage of a lake breeze front. Due to the strong convection and cumulus clouds in the vicinity for much of the day, VCD_{RTM} could not be determined until after 17:00 EDT. Winds that were from the W-SW (260°) at 9 $m\,s^{-1}$, switched to S–SW (215°) at 13 $m\,s^{-1}$ with gusts up to 17 $m\,s^{-1}$ at 15:10 EDT, indicating the passage of the highly deformed lake breeze front (Lake Erie), and accompanied with an increase in relative humidity, spikes in O_3, $PM_{2.5}$, CO (not shown), and a drop in NO_2. Between 17:00 and 19:15 EDT, conditions were hazy but cloud-free such that estimates of VCD_{RTM} were determinable. The NO_2 was relatively low, between 0.5 and 1.5 ppb, while VCDs ranged from 2–4×10^{15} molec cm^{-2}, and BL_{eff} increased from 800 m to 2600 m at 17:10 EDT. The DSCDs do not give any indication of an elevated plume, and a measure of the true boundary layer height was not available at Ridgetown on this day. However, the potential temperature profile measured by sonde release at White Lake,

Michigan, just west of Detroit (Station DTX, #72632), indicated a subsidence inversion at 1.90 km at 20:00 EDT, that was comparable to the average BL_{eff} measured between 16:00 and 17:10 EDT (1.93 km). Thus, on this particular day, when strong wind speeds and strong convection would support a well mixed boundary layer, the value of BL_{eff} was comparable to the true boundary layer height measured in a continental region close to the site. This is one of the few situations during the study where we expect this to be true. In such a case, the mixing ratio of NO_2 measured at ground level is quite low, and may not indicate the total amount of NO_2 being transported into the region in the deep boundary layer. To estimate the total transport of tropospheric NO_2 across a boundary tangential to the wind direction during this pollution event, the flux of tropospheric NO_2 perpendicular to the wind direction, F_{NO_2} (molec s^{-1}), could be calculated according the following equation:

$$F_{NO_2} = VCD_{NO_2} \times L \times u_{trop} \quad (18)$$

where L is the length of a border, and u_{trop} is the average flow rate of the troposphere. Using the wind speed at 10 m height (12 $m\,s^{-1}$ in late afternoon) as a lower limit of the flow rate in the lower troposphere, and the average VCD_{RTM} in the later afternoon period (3.4 × 10^{15} molec cm^{-2}), we conservatively estimate the line flux (F_{NO_2}/L) of NO_2 through the region to be greater than 4.1 × 10^{18} molec $cm^{-1}\,s^{-1}$, or 112 kg $NO_2\,km^{-1}\,h^{-1}$, during the pollution event. This may be a useful parameter to compare with model estimates of transport fluxes where they exist.

5 Conclusions

We outline a method for the determination of aerosol optical depths and vertical column densities of NO_2 using a combination of MAX-DOAS measurement of NO_2 and O_4, radiative transfer and inversion modeling. The aerosol optical depths (λ = 360 nm) determined with this method were compared to other measures of aerosol optical depth

regionally available (OMI, MODIS, AERONET) with some qualitative agreement, although differences in the wavelengths used and spatial locations prevented a more direct comparison of these measures. A direct comparison between τ_{RTM} and $PM_{2.5}$ measured at the site gave a very low level of correlation, while a direct comparison between the calculated aerosol extinction coefficient (τ_{RTM}/H_{aer}) and $PM_{2.5}$ gave a much higher correlation and a slope of $53 \pm 10\,\mu g\,m^{-3}$ km. This emphasizes the importance of taking into account boundary layer heights in any attempts to link aerosol optical depths determined by satellite, for example, with human exposure of aerosols at ground level.

The tropospheric VCDs of NO_2 derived this way, VCD_{RTM}, were compared to tropospheric VCDs compiled through vertical measurements of NO_2 close to the site, VCD_{COMP}. On average, VCD_{RTM} was 15% higher than VCD_{COMP}, but the difference was not statistically significant, which was taken as a validation for the method outlined here for determining VCDs of NO_2. Intercomparison of satellite instrument derived VCDs with a limited number of comparison points from OMI ($N = 8$) and SCIAMACHY ($N = 1$) indicate that the satellite derived measures were ~50% higher than VCD_{RTM}, with a mean error of $0.5 - 0.9 \times 10^{15}$ molec cm^{-2}.

Previous literature has reported the opposite, namely that satellite derived measures of VCD are on average smaller than VCDs found via MAX-DOAS. The root cause for these differences is probably the different nature of the measurement sites; rural in this study compared to more urban in previous reports, or the overall values of the VCD of NO_2 which were much lower in this study compared to previous reports. Typically, VCDs derived from MAX-DOAS in previous comparisons with satellite measures of NO_2 have used a geometrical approximation to estimate the air mass factor and VCD, similar to the VCD_{GEO} values reported here. Our VCD_{GEO} values were marginally lower than our VCD_{RTM} values, but only for a small subset of comparisons with a stringent criteria, namely that the VCDs determined using a geometric approximation with elevation angles of 10° and 30° agree to within 15%. The methodology we outlined here to determine VCD_{RTM} is not as stringent, and has allowed us to determine VCDs over a much wider range of aerosol conditions than would otherwise be possible using just

the geometric approximation.

We define the ratio of the tropospheric VCD and ground level concentration of NO_2 to be the effective boundary layer height, BL_{eff}. The diurnal pattern of BL_{eff} generally follows the expected pattern for the boundary layer height during the day; although we find values of BL_{eff} are generally lower than expected for continental boundary layer heights in late afternoon, likely due to surface sources in a boundary layer that is not well mixed. We illustrate exceptions to this in three case studies. In two of the cases, we show high values of BL_{eff} are due to elevated plumes of NO_2, one from elevated stack emissions from industry, and one from biomass burning plumes that were transported through the region. In the third case, we found that BL_{eff} was very high (~2 km) and similar to the measured continental boundary layer height just west of the study region, likely as a result of instability in the atmosphere that promoted convection and efficient mixing throughout the boundary layer. The variations of BL_{eff} with time of day and conditions, should be considered in attempts to determine ground level concentrations of NO_2 from satellite derived measures, or in attempts to validate satellite measurements through use of ground-based measurements.

The case studies examined here also provide some interesting examples of transport of pollutants in this region and the interaction with lake breezes that exist due to the presence of the surrounding lakes. In our first case study, we present a convincing example of fumigation of elevated industrial pollutants brought to the surface at a lake breeze front, and an increase in the total VCD of NO_2 at the lake breeze front. Our last case study occurred during a regional smog event with transport of ozone and aerosol precursors from the southwest. Although ground level concentrations of NO_2 were quite low during this event (<1.5 ppb), the column amount of NO_2 was more substantial than otherwise suspected due to a deep and well mixed boundary layer. We have estimated the line flux of NO_2, at this time, to be greater than 112 kg NO_2 km^{-1} h^{-1}. Multiplication of the line flux by the width of a boundary line perpendicular to the prevailing wind direction would give the total mass transport of tropospheric NO_2 across the boundary line, during the regional pollution event.

Acknowledgements. The authors wish to acknowledge funding from NSERC and from a grant provided by the Ontario Ministry of the Environment. LIDAR information was provided by B. Firanski and K. Strawbridge, Environment Canada. OMI data was obtained and processed through joint research between the Netherlands (NIVR/KNMI), Finland (FMI), and the US (NASA) in the Earth Observing System (EOS) Aura Mission, J. P. Veefkind (KNMI) and J. F. Gleason (NASA), Principal Investigators. For AERONET data (Egbert), technical support was provided by I. Abboud of Environment Canada and J. Freemantle of the Universite de Sherbrooke, while N. O'Neill and B. McArthur were the scientific principal investigators. For AERONET data (Kellogg), P. Robertson was the principal investigator. Thanks to T. Deutschmann, the developer of the McArtim RTM, E. Celarier and I. Levy for helpful discussions, and C. Weldon and P. Wojtal for proofreading the manuscript.

References

Alicke, B., Geyer, A., Hofzumahaus, A., Holland, F., Konrad, S., Patz, H. W., Schafer, J., Stutz, J., Volz-Thomas, A., and Platt, U.: OH formation by HONO photolysis during the BERLIOZ experiment, J. Geophys. Res.-Atmos., 108, 8247, doi:10.1029/2001JD000579, 2003. 13037

Beirle, S., Kühl, S., Pukīte, J., and Wagner, T.: Retrieval of tropospheric column densities of NO_2 from combined SCIAMACHY nadir/limb measurements, Atmos. Meas. Tech., 3, 283–299, doi:10.5194/amt-3-283-2010,1 2010. 13043

Blond, N., Boersma, K. F., Eskes, H. J., van der A, R. J., Roozendael, M. V., Smedt, I. D., Bergametti, G., and Vautard, R.: Intercomparison of SCIAMACHY nitrogen dioxide observations, in situ measurements and air quality modeling results over Western Europe, J. Geophys. Res.-Atmos., 112, D10311, doi:10.1029/2006JD007277, 2007. 13055

Boersma, K. F., Bucsela, E. J., Brinksma, E. J., and Gleason, J. F.: NO_2, OMI-EOS Algorithm, Theoretical Basis Document: Trace Gas Algorithms: NO_2, 12–35, 2001. 13044

Bogumil, K., Orphal, J., Homann, T., Voigt, S., Spietz, P., Fleischmann, O. C., Vogel, A., Hartmann, M., Kromminga, H., Bovensmann, H., Frerick, J., and Burrows, J. P.: Measurements of molecular absorption spectra with the SCIAMACHY pre-flight model: instrument characterization and reference data for atmospheric remote-sensing in the 230–2380 nm region, J. Photoch. Photobio. A, 157, 167–184, 2003. 13042

Bovensmann, H., Burrows, J. P., Buchwitz, M., Frerick, J., Noel, S., Rozanov, V. V., Chance, K. V., and Goede, A. P. H.: SCIAMACHY: Mission objectives and measurement modes, J. Atmos. Sci., 56, 127–150, 1999. 13038, 13043

Brinksma, E. J., Pinardi, G., Volten, H., Braak, R., Richter, A., Schoenhardt, A., van Roozendael, M., Fayt, C., Hermans, C., Dirksen, R. J., Vlemmix, T., Berkhout, A. J. C., Swart, D. P. J., Oetjen, H., Wittrock, F., Wagner, T., Ibrahim, O. W., de Leeuw, G., Moerman, M., Curier, R. L., Celarier, E. A., Cede, A., Knap, W. H., Veefkind, J. P., Eskes, H. J., Allaart, M., Rothe, R., Piters, A. J. M., and Levelt, P. F.: The 2005 and 2006 DANDELIONS NO_2 and aerosol intercomparison campaigns, J. Geophys. Res.-Atmos., 113, D16S46, doi:10.1029/2007JD008808, 2008. 13039, 13047, 13058, 13059

Bucsela, E., Celarier, E., Wenig, M., Gleason, J., Veefkind, J., Boersma, K. F., and Brinksma, E.: Algorithm for NO_2 vertical column retrieval from the Ozone Monitoring Instrument, IEEE T. Geosci. Remote, 44, 1245–1258, 2006. 13044

Burrows, J. P., Richter, A., Dehn, A., Deters, B., Himmelmann, S., and Orphal, J.: Atmospheric remote-sensing reference data from GOME 2. Temperature-dependent absorption cross sections of O_3 in the 231–794 nm range, J. Quant. Spectrosc. Ra., 61, 509–517, 1999. 13044

Celarier, E. A., Brinksma, E. J., Gleason, J. F., Veefkind, J. P., Cede, A., Herman, J. R., Ionov, D., Goutail, F., Pommereau, J. P., Lambert, J. C., Roozendael, M. V., Pinardi, G., Wittrock, F., Schoenhardt, A., Richter, A., Ibrahim, O. W., Wagner, T., Bojkov, B., Mount, G., Spinei, E., Chen, C. M., Pongetti, T. J., Sander, S. P., Bucsela, E. J., Wenig, M. O., Swart, D. P. J., Volten, H., Kroon, M., and Levelt, P. F.: Validation of ozone monitoring instrument nitrogen dioxide columns, J. Geophys. Res.-Atmos., 113, D15S15, doi:10.1029/2007JD008908, 2008. 13038, 13039, 13044, 13058

Chance, K. V. and Spurr, R. J. D.: Ring effect studies: Rayleigh scattering, including molecular parameters for rotational Raman scattering, and the Fraunhofer spectrum, Appl. Optics, 36, 5224–5230, 1997. 13044

Chen, D., Zhou, B., Beirle, S., Chen, L. M., and Wagner, T.: Tropospheric NO_2 column densities deduced from zenith-sky DOAS measurements in Shanghai, China, and their application to satellite validation, Atmos. Chem. Phys., 9, 3641–3662, doi:10.5194/acp-9-3641-2009, 2009. 13039, 13043, 13058

Chu, D. A., Kaufman, Y. J., Zibordi, G., Chern, J. D., Mao, J., Li, C. C., and Holben, B. N.: Global monitoring of air pollution over land from the Earth Observing System-Terra Moderate Resolution Imaging Spectroradiometer (MODIS), J. Geophys. Res.-Atmos., 108, 4661,

doi:10.1029/2002JD003179, 2003. 13053
Clémer, K., Van Roozendael, M., Fayt, C., Hendrick, F., Hermans, C., Pinardi, G., Spurr, R., Wang, P., and De Maziére, M.: Multiple wavelength retrieval of tropospheric aerosol optical properties from MAXDOAS measurements in Beijing, Atmos. Meas. Tech., 3, 863–878, doi:10.5194/amt-3-863-2010, 2010. 13039
Dentener, F. J. and Crutzen, P. J.: Reaction of N_2O_5 on Tropospheric Aerosols – Impact on the Global Distributions of NO_X, O_3, and OH, J. Geophys. Res.-Atmos., 98, 7149–7163, 1993. 13037
Deutschmann, T., Beirle, S., Frieß, U., Grzegorski, M., Kern, C., Kritten, L., Platt, U., Prados-Román, C., Puķīte, J., Wagner, T., Werner, B., and Pfeilsticker, K.: The Monte carlo Atmospheric radiative transfer model McArtim: Introduction and validation of Jacobians and 3-D features, J. Quant. Spectrosc.Ra., 112, 1119–1137, 2011. 13043, 13048
Dubovik, O. and King, M. D.: A flexible inversion algorithm for retrieval of aerosol optical properties from Sun and sky radiance measurements, J. Geophys. Res.-Atmos., 105, 20673–20696, 2000. 13045
EC: Environment Canada, National Pollutant Release Inventory, available at: http://www.ec.gc.ca/inrp-npri/default.asp?lang=En&n=4A577BB9-%1, 2011. 13065
Engel-Cox, J. A., Holloman, C. H., Coutant, B. W., and Hoff, R. M.: Qualitative and quantitative evaluation of MODIS satellite sensor data for regional and urban scale air quality, Atmos. Environ., 38, 2495–2509, 2004. 13053
Engel-Cox, J. A., Hoff, R. M., Rogers, R., Dimmick, F., Rush, A. C., Szykman, J. J., Al-Saadi, J., Chu, D. A., and Zell, E. R.: Integrating lidar and satellite optical depth with ambient monitoring for 3-dimensional particulate characterization, Atmos. Environ., 40, 8056–8067, 2006. 13053
Fayt, C. and Roozendael, M. V.: WinDOAS 2.1 – 2001, available at: http://bro.aeronomie.be/WinDOAS-SUM-210b.pdf, 2011. 13041
Finlayson-Pitts, B. J. and Pitts, J. N.: Chemistry of the Upper and Lower Atmosphere, Academic Press, San Diego, California, 1999. 13037
Frieß, U., Monks, P. S., Remedios, J. J., Rozanov, A., Sinreich, R., Wagner, T., and Platt, U.: MAX-DOAS O_4 measurements: A new technique to derive information on atmospheric aerosols: 2. Modeling studies, J. Geophys. Res.-Atmos., 111, D14203, doi:10.1029/2005JD006618, 2006. 13047, 13048, 13059
Grainger, J. F. and Ring, J.: Anomalous Fraunhofer Line Profiles, Nature, 193, 762, 1962.

13042
Greenblatt, G. D., Orlando, J. J., Burkholder, J. B., and Ravishankara, A. R.: Absorption-Measurements of Oxygen between 330 nm and 1140 nm, J. Geophys. Res.-Atmos., 95, 18577–18582, 1990. 13042
Gupta, P. and Christopher, S. A.: Seven year particulate matter air quality assessment from surface and satellite measurements, Atmos. Chem. Phys., 8, 3311–3324, doi:10.5194/acp-8-3311-2008, 2008. 13053
Harder, J. W. and Brault, J. W.: Atmospheric measurements of water vapor in the 442-nm region, J. Geophys. Res.-Atmos., 102, 6245–6252, 1997. 13044
Hastie, D. R., Narayan, J., Schiller, C., Niki, H., Shepson, P. B., Sills, D. M. L., Taylor, P. A., Moroz, W. J., Drummond, J. W., Reid, N., Taylor, R., Roussel, P. B., and Melo, O. T.: Observational evidence for the impact of the lake breeze circulation on ozone concentrations in Southern Ontario, Atmos. Environ., 33, 323–335, 1999. 13040
Hayden, K., Sills, D., Brook, J., Li, S., Makar, P., Markovic, M., Liu, P., Anlauf, K., O'Brien, J., Lin, Q., and McLaren, R.: Aircraft study of the impact of lake-breeze circulations on trace gases and particles during BAQS-Met 2007, Atmos. Chem. Phys. Discuss., 11, 11497-11546, 2011,
http://www.atmos-chem-phys-discuss.net/11/11497/2011/. 13046
Heckel, A., Richter, A., Tarsu, T., Wittrock, F., Hak, C., Pundt, I., Junkermann, W., and Burrows, J. P.: MAX-DOAS measurements of formaldehyde in the Po-Valley, Atmos. Chem. Phys., 5, 909–918, doi:10.5194/acp-5-909-2005, 2005. 13039
Heland, J., Schlager, H., Richter, A., and Burrows, J. P.: First comparison of tropospheric NO_2 column densities retrieved from GOME measurements and in situ aircraft profile measurements, Geophy. Res. Lett., 29, 1983, doi:10.1029/2002GL015528, 2002. 13056
Hendrick, F., Van Roozendael, M., Kylling, A., Petritoli, A., Rozanov, A., Sanghavi, S., Schofield, R., von Friedeburg, C., Wagner, T., Wittrock, F., Fonteyn, D., and De Maziére, M.: Intercomparison exercise between different radiative transfer models used for the interpretation of ground-based zenith-sky and multi-axis DOAS observations, Atmos. Chem. Phys., 6, 93–108, doi:10.5194/acp-6-93-2006, 2006. 13047, 13048
Holben, B. N., Eck, T. F., Slutsker, I., Tanre, D., Buis, J. P., Setzer, A., Vermote, E., Reagan, J. A., Kaufman, Y. J., Nakajima, T., Lavenu, F., Jankowiak, I., and Smirnov, A.: AERONET – A federated instrument network and data archive for aerosol characterization, Remote Sens. Environ., 66, 1–16, 1998. 13045

Holben, B. N., Tanre, D., Smirnov, A., Eck, T. F., Slutsker, I., Abuhassan, N., Newcomb, W. W., Schafer, J. S., Chatenet, B., Lavenu, F., Kaufman, Y. J., Castle, J. V., Setzer, A., Markham, B., Clark, D., Frouin, R., Halthore, R., Karneli, A., O'Neill, N. T., Pietras, C., Pinker, R. T., Voss, K., and Zibordi, G.: An emerging ground-based aerosol climatology: Aerosol optical depth from AERONET, J. Geophys. Res.-Atmos., 106, 12067–12097, 2001. 13045

Hönninger, G., von Friedeburg, C., and Platt, U.: Multi axis differential optical absorption spectroscopy (MAX-DOAS), Atmos. Chem. Phys., 4, 231–254, doi:10.5194/acp-4-231-2004, 2004. 13038, 13064

Irie, H., Kanaya, Y., Akimoto, H., Iwabuchi, H., Shimizu, A., and Aoki, K.: First retrieval of tropospheric aerosol profiles using MAX-DOAS and comparison with lidar and sky radiometer measurements, Atmos. Chem. Phys., 8, 341–350, doi:10.5194/acp-8-341-2008, 2008. 13039, 13053

Irie, H., Kanaya, Y., Akimoto, H., Iwabuchi, H., Shimizu, A., and Aoki, K.: Dual-wavelength aerosol vertical profile measurements by MAX-DOAS at Tsukuba, Japan, Atmos. Chem. Phys., 9, 2741–2749, doi:10.5194/acp-9-2741-2009, 2009. 13039, 13056, 13058

Kacenelenbogen, M., Léon, J.-F., Chiapello, I., and Tanré, D.: Characterization of aerosol pollution events in France using ground-based and POLDER-2 satellite data, Atmos. Chem. Phys., 6, 4843–4849, doi:10.5194/acp-6-4843-2006, 2006. 13053

Koelemeijer, R. B. A., Homan, C. D., and Matthijsen, J.: Comparison of spatial and temporal variations of aerosol optical thickness and particulate matter over Europe, Atmos. Environ., 40, 5304–5315, 2006. 13053

Kraus, S.: DOASIS, A Framework Design for DOAS, Ph.D. thesis, University of Heidelberg, 2006. 13042

Kurucz, R. L., Furenlid, I. J., and Testerman, L.: Solar Flux Atlas from 296 to 1300 nm, National Solar Observatory, Tech. rep., 1984. 13041

Ladstätter-Weißenmayer, A., Heland, J., Kormann, R., von Kuhlmann, R., Lawrence, M. G., Meyer-Arnek, J., Richter, A., Wittrock, F., Ziereis, H., and Burrows, J. P.: Transport and build-up of tropospheric trace gases during the MINOS campaign: comparision of GOME, in situ aircraft measurements and MATCH-MPIC-data, Atmos. Chem. Phys., 3, 1887–1902, doi:10.5194/acp-3-1887-2003, 2003. 13056

Lee, H., Irie, H., Kim, Y. J., Noh, Y., Lee, C., Kim, Y., and Chun, K. J.: Retrieval of Aerosol Extinction in the Lower Troposphere Based on UV MAX-DOAS Measurements, Aerosol Sci. Technol., 43, 502–509, 2009. 13039, 13053

Levelt, P. F., den Oord, G. H. J. V., Dobber, M. R., Malkki, A., Visser, H., de Vries, J., Stammes, P., Lundell, J. O. V., and Saari, H.: The Ozone Monitoring Instrument, IEEE T. Geosci. Remote, 44, 1093–1101, 2006. 13038, 13044

Levy, R. C., Remer, L. A., and Dubovik, O.: Global aerosol optical properties and application to Moderate Resolution Imaging Spectroradiometer aerosol retrieval over land, J. Geophys. Res.-Atmos., 112, D13210, doi:10.1029/2006JD007815, 2007. 13045

Li, X., Brauers, T., Shao, M., Garland, R. M., Wagner, T., Deutschmann, T., and Wahner, A.: MAX-DOAS measurements in southern China: retrieval of aerosol extinctions and validation using ground-based in-situ data, Atmos. Chem. Phys., 10, 2079–2089, doi:10.5194/acp-10-2079-2010, 2010. 13039, 13048, 13049

Lyons, W. A. and Cole, H. S.: Fumigation and Plume Trapping on the Shores of Lake Michigan During Stable Onshore Flow, J. Appl. Meteorol., 12, 494–510, 1973. 13065, 13066

Martin, R. V., Chance, K., Jacob, D. J., Kurosu, T. P., Spurr, R. J. D., Bucsela, E., Gleason, J. F., Palmer, P. I., Bey, I., Fiore, A. M., Li, Q., Yantosca, R. M., and Koelemeijer, R. B. A.: An improved retrieval of tropospheric nitrogen dioxide from GOME, J. Geophys. Res., 107, 4437, doi:10.1029/2001JD001027, 2002. 13038

McLaren, R., Salmon, R. A., Liggio, J., Hayden, K. L., Anlauf, K. G., and Leaitch, W. R.: Nighttime chemistry at a rural site in the Lower Fraser Valley, Atmos. Environ., 38, 5837–5848, 2004. 13037

McLaren, R., Wojtal, P., Majonis, D., McCourt, J., Halla, J. D., and Brook, J.: NO_3 radical measurements in a polluted marine environment: links to ozone formation, Atmos. Chem. Phys., 10, 4187–4206, doi:10.5194/acp-10-4187-2010, 2010. 13042

MOE: Ministry of the Environment, Ontario (MOE): Air Quality in Ontario 2005 Report and Appendix, available at: http://www.ene.gov.on.ca/environment/en/resources/STD01_076445.html, 2011. 13067

Müller, J. F.: Geographical-Distribution and Seasonal-Variation of Surface Emissions and Deposition Velocities of Atmospheric Trace Gases, J. Geophys. Res.-Atmos., 97, 3787–3804, 1992. 13037

NASA: NASA Goddard Space Flight Center LAADS Web – Level 1 and Atmosphere Archive and Distribution System, available at: http://ladsweb.nascom.nasa.gov/, 2010a. 13045

NASA: NASA Goddard Space Flight Center Aura Validation Data Center, available at: http://avdc.gsfc.nasa.gov/, 2010b. 13044, 13045

NASA: NASA Goddard Space Flight Center AERONET – Aerosol Robotic Network, available

at: http://aeronet.gsfc.nasa.gov/, 2010c. 13045
Pelletier, B., Santer, R., and Vidot, J.: Retrieving of particulate matter from optical measurements: A semiparametric approach, J. Geophys. Res.-Atmos., 112, D06208, doi:10.1029/2005JD006737, 2007. 13053
Perliski, L. M. and Solomon, S.: On the Evaluation of Air-Mass Factors for Atmospheric Near-Ultraviolet and Visible Absorption-Spectroscopy, J. Geophys. Res.-Atmos., 98, 10363–10374, 1993. 13038, 13046
Plane, J. M. C. and Smith, N.: Atmospheric Monitoring By Differential Optical Absorption Spectroscopy, vol. 24 of Spectroscopy in Environmental Science, chap. Chapter 5, p. 223, John Wiley & Sons, Inc., West Sussex, England, 1995. 13041
Platt, U.: Differential Optical Absorption Spectroscopy (DOAS), vol. 127 of Air Monitoring by Spectroscopic Technique, Chemical Analysis Series, p. 27, John Wiley & Sons, Inc., Hoboken, N.J., 1994. 13041
Platt, U. and Perner, D.: Direct Measurements of Atmospheric CH_2O, HNO_2, O_3, NO_2, and SO_2 by Differential Optical Absorption in the Near UV, J. Geophys. Res., 85, 7453–7458, 1980. 13037
Platt, U. and Stutz, J.: Differential Optical Absorption Spectroscopy: Principles and Applications, Springer, Berlin, Heidelberg, Germany, 2008. 13037, 13041, 13043, 13044
Reid, N. W., Niki, H., Hastie, D., Shepson, P., Roussel, P., Melo, O., Mackay, G., Drummond, J., Schiff, H., Poissant, L., and Moroz, W.: The southern Ontario oxidant study (SONTOS): Overview and case studies for 1992, Atmos. Environ., 30, 2125–2132, 1996. 13040
Schaap, M., Apituley, A., Timmermans, R. M. A., Koelemeijer, R. B. A., and de Leeuw, G.: Exploring the relation between aerosol optical depth and $PM_{2.5}$ at Cabauw, the Netherlands, Atmos. Chem. Phys., 9, 909–925, doi:10.5194/acp-9-909-2009, 2009. 13053
Sills, D. M. L., Brook, J. R., Levy, I., Makar, P. A., Zhang, J., and Taylor, P. A.: Lake breezes in the southern Great Lakes region and their influence during BAQS-Met 2007, Atmos. Chem. Phys. Discuss., 11, 3579–3626, doi:10.5194/acpd-11-3579-2011, 2011. 13040, 13063, 13064, 13065, 13066, 13067
Sinreich, R., Friess, U., Wagner, T., and Platt, U.: Multi axis differential optical absorption spectroscopy (MAX-DOAS) of gas and aerosol distributions, Faraday Discuss., 130, 153–164, 2005. 13047
Solomon, S., Schmeltekopf, A. L., and Sanders, R. W.: On the Interpretation of Zenith Sky Absorption Measurements, J. Geophys. Res., 92, 8311–8319, 1987. 13038, 13046

Torres, O., Bhartia, P. K., Herman, J. R., Ahmad, Z., and Gleason, J.: Derivation of aerosol properties from satellite measurements of backscattered ultraviolet radiation: Theoretical basis, J. Geophys. Res.-Atmos., 103, 17099–17110, 1998. 13045
UWYO: University of Wyoming (UWYO), College of Engineering, Department of Atmospheric Science Atmospheric Soundings, available at: http://weather.uwyo.edu/upperair/sounding.html, 2010. 13048
Vandaele, A. C., Hermans, C., Simon, P. C., Carleer, M., Colin, R., Fally, S., Merienne, M. F., Jenouvrier, A., and Coquart, B.: Measurements of the NO_2 absorption cross-section from 42 000 cm^{-1} to 10 000 cm^{-1} (238–1000 nm) at 220 K and 294 K, J. Quant. Spectrosc. Ra., 59, 171–184, 1998. 13042, 13044
Wagner, T., von Friedeburg, C., Wenig, M., Otten, C., and Platt, U.: UV-visible observations of atmospheric O_4 absorptions using direct moonlight and zenith-scattered sunlight for clear-sky and cloudy sky conditions, J. Geophys. Res.-Atmos., 107, 4424, doi:10.1029/2001JD001026, 2002. 13048
Wagner, T., Dix, B., von Friedeburg, C., Friess, U., Sanghavi, S., Sinreich, R., and Platt, U.: MAX-DOAS O_4 measurements: A new technique to derive information on atmospheric aerosols – Principles and information content, J. Geophys. Res.-Atmos., 109, D22205, doi:10.1029/2004JD004904, 2004. 13048
Wagner, T., Burrows, J. P., Deutschmann, T., Dix, B., von Friedeburg, C., Frieß, U., Hendrick, F., Heue, K.-P., Irie, H., Iwabuchi, H., Kanaya, Y., Keller, J., McLinden, C. A., Oetjen, H., Palazzi, E., Petritoli, A., Platt, U., Postylyakov, O., Pukite, J., Richter, A., van Roozendael, M., Rozanov, A., Rozanov, V., Sinreich, R., Sanghavi, S., and Wittrock, F.: Comparison of box-air-mass-factors and radiances for Multiple-Axis Differential Optical Absorption Spectroscopy (MAX-DOAS) geometries calculated from different UV/visible radiative transfer models, Atmos. Chem. Phys., 7, 1809–1833, doi:10.5194/acp-7-1809-2007, 2007. 13047, 13048
Wagner, T., Deutschmann, T., and Platt, U.: Determination of aerosol properties from MAX-DOAS observations of the Ring effect, Atmos. Meas. Tech., 2, 495–512, doi:10.5194/amt-2-495-2009, 2009. 13048
Wagner, T., Beirle, S., Brauers, T., Deutschmann, T., Frieß, U., Hak, C., Halla, J., Heue, K., Junkermann, W., Li, X., Platt, U., and Pundt, I.: Inversion of tropospheric profiles of aerosol extinction and HCHO and NO_2 concentrations from MAX-DOAS observations in Milano in summer 2003 and comparison with independent data sets, Atmos. Meas. Tech. Discuss., in preparation, 2011. 13039, 13049, 13052

Wang, J. and Christopher, S. A.: Intercomparison between satellite-derived aerosol optical thickness and $PM_{2.5}$ mass: Implications for air quality studies, Geophys. Res. Lett., 30, 2095, doi:10.1029/2003GL018174, 2003. 13053

Wenig, M. O., Cede, A. M., Bucsela, E. J., Celarier, E. A., Boersma, K. F., Veefkind, J. P., Brinksma, E. J., Gleason, J. F., and Herman, J. R.: Validation of OMI tropospheric NO_2 column densities using direct-Sun mode Brewer measurements at NASA Goddard Space Flight Center, J. Geophys. Res.-Atmos., 113, D16S45, doi:10.1029/2007JD008988, 2008. 13044, 13059

Wittrock, F., Oetjen, H., Richter, A., Fietkau, S., Medeke, T., Rozanov, A., and Burrows, J. P.: MAX-DOAS measurements of atmospheric trace gases in Ny-Ålesund – Radiative transfer studies and their application, Atmos. Chem. Phys., 4, 955–966, doi:10.5194/acp-4-955-2004, 2004. 13039, 13048

Zieger, P., Weingartner, E., Henzing, J., Moerman, M., de Leeuw, G., Mikkilä, J., Ehn, M., Petäjä, T., Clémer, K., van Roozendael, M., Yilmaz, S., Frieß, U., Irie, H., Wagner, T., Shaiganfar, R., Beirle, S., Apituley, A., Wilson, K., and Baltensperger, U.: Comparison of ambient aerosol extinction coefficients obtained from in-situ, MAX-DOAS and LIDAR measurements at Cabauw, Atmos. Chem. Phys., 11, 2603–2624, doi:10.5194/acp-11-2603-2011, 2011. 13049, 13052

Table 1. Comparison of RTM and composite VCDs of NO_2 on 26 June 2007.

Point	Time (EDT)	VCD^{*}_{COMP} (10^{15} molec cm^{-2})	VCD^{*}_{RTM} (10^{15} molec cm^{-2})	Error (10^{15} molec cm^{-2})	VCD^{*}_{RTM} vs. VCD_{COMP}
1	08:31–08:57	4.06 ± 1.11	5.84 ± 1.92	1.78	
2	09:03–09:29	3.85 ± 1.19	4.18 ± 1.37	0.33	
3	17:25–17:46	3.06 ± 1.22	2.59 ± 0.93	−0.47	
4	17:52–18:15	3.18 ± 1.22	3.50 ± 1.25	0.32	
Mean		3.54 ± 0.59	4.03 ± 0.71	0.49	1.14 ± 0.27
RMSE				0.95	
				Slope (forced zero intercept)	1.16 ± 0.12 (0.39)
				Correlation, R	0.77

* All uncertainties are standard (1σ) except those in brackets, which are at the 95% confidence level.

Table 2. Comparison of various NO_2 VCDs to the values of VCD_{RTM}.

	OMI AURA*	SCIAMACHY ENVISAT	Geometric Approximation*	Aircraft Composite*
Number of Data Pairs, N	8	1	10	4
$VCD_{measured}$ ($\times 10^{15}$ molec cm^{-2})	2.67	1.39	1.88	3.54
$\overline{VCD_{RTM}}$ ($\times 10^{15}$ molec cm^{-2})	1.76	0.916	2.05	4.03
$VCD_{measured}/\overline{VCD_{RTM}}$	1.52 ± 0.12 (0.25)	1.5	0.92 ± 0.07 (0.15)	0.88 ± 0.09 (0.19)
Slope (forced zero intercept)	1.47 ± 0.20 (0.47)	N/A	0.88 ± 0.04 (0.09)	0.83 ± 0.09 (0.28)
Mean Error ($\times 10^{15}$ molec cm^{-2})	0.91	0.48	−0.17	−0.49
RMSE ($\times 10^{15}$ molec cm^{-2})	1.33	N/A	0.41	0.95
Correlation, R	0.63	N/A	0.97	0.77

* All uncertainties are standard (1σ) except those in brackets, which are at the 95% confidence level.

Table 3. Average VCD_{RTM}, ground NO_2, and BL_{eff} for selected time periods at Ridgetown.

Time Period (EDT)	VCD_{RTM} ($\times 10^{15}$ molec cm^{-2})	n_{NO_2} ($\times 10^{15}$ molec cm^{-3})	BL_{eff} (m)
06:00–09:00	2.4 ± 0.8	21.4 ± 3.2	119 ± 45
09:00–12:00	2.1 ± 0.7	10.6 ± 1.7	203 ± 77
12:00–16:00	1.5 ± 0.5	6.4 ± 1.0	201 ± 77
16:00–20:00	2.7 ± 0.9	7.1 ± 1.0	521 ± 198

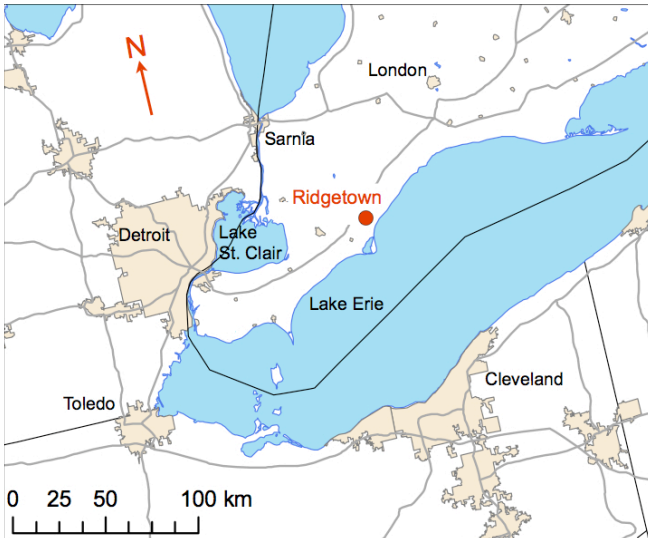

Fig. 1. BAQS-Met field study Ridgetown supersite and other areas of interest in southwestern Ontario and adjacent areas in the USA.

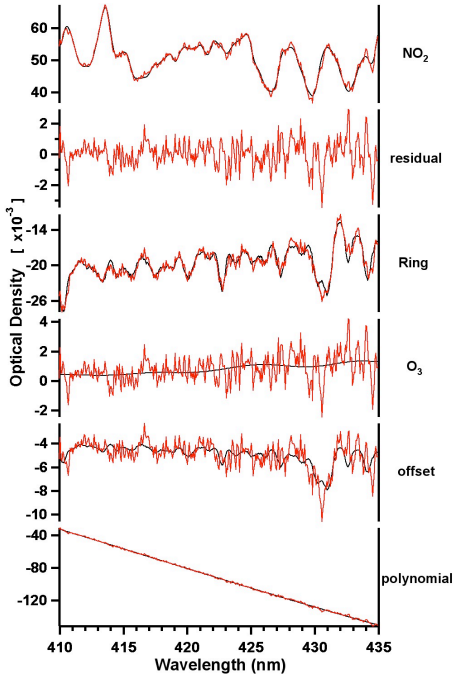

Fig. 2. NO_2 MAX-DOAS fit retrieval for a measurement with $\alpha = 4^{\circ}$ on 20 June 2007, 09:46 EDT. This fit, performed between 410–435 nm, includes the NO_2 and O_3 absorption cross sections, plus a 3rd order polynomial, offset polynomial, FRS, and Ring. The residual of the fit is shown in the second panel. For each remaining panel the black line represents the DOAS fit, and the red line represents the DOAS fit plus the residual of the species examined.

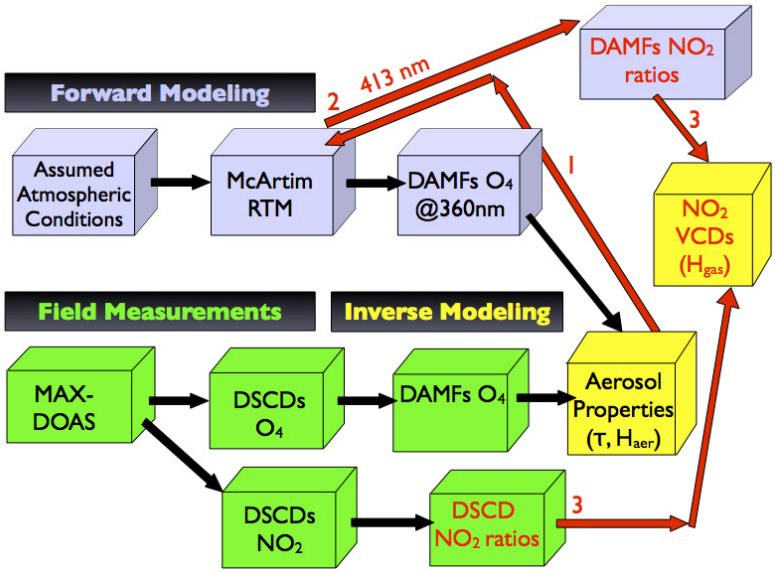

Fig. 3. Flowchart of methodology for determination of NO_2 VCDs and aerosol properties from MAX-DOAS measurements, RTM and inverse modeling. Measurements in green boxes represent products obtained from direct MAX-DOAS measurements in the field, while parameters and products shown in the grey boxes represent modeled quantities and results only. The quantities in the yellow boxes are obtained from inverse modeling.

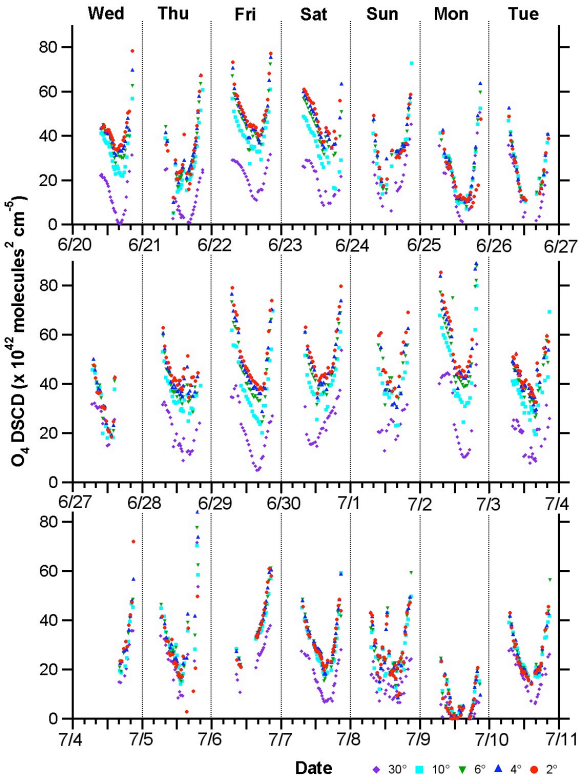

Fig. 4. O_4 DSCDs for cloud-free conditions during the BAQS-Met campaign at the Ridgetown supersite. Major ticks represent 12 midnight and 12 noon EDT, while minor ticks indicate every 4-h increment.

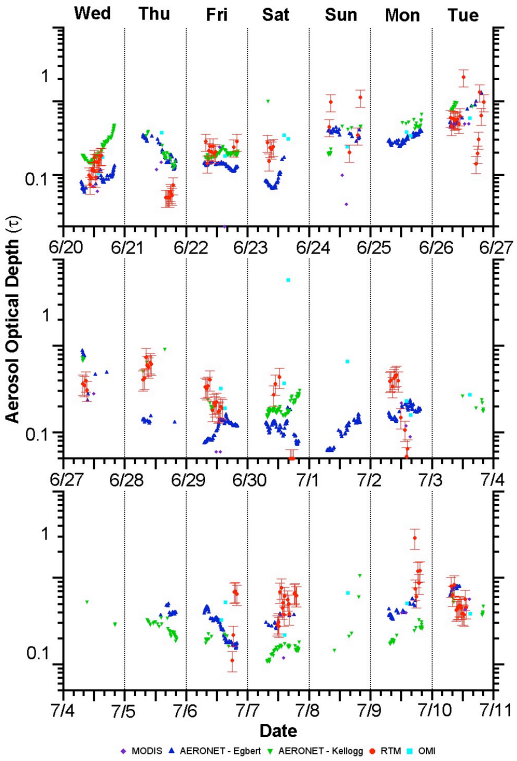

Fig. 5. Aerosol optical depth for the entire BAQS-Met campaign. For AERONET locations (Egbert, Kellogg) $\lambda_{avg} = 360$ nm, for coincident satellite measurements (OMI $\lambda = 388$ nm, MODIS $\lambda = 550$ nm), and for the MAX-DOAS-RTM values at Ridgetown, $\lambda = 360$ nm. Major ticks represent 12 midnight and 12 noon EDT, while minor ticks indicate every 4-h increment.

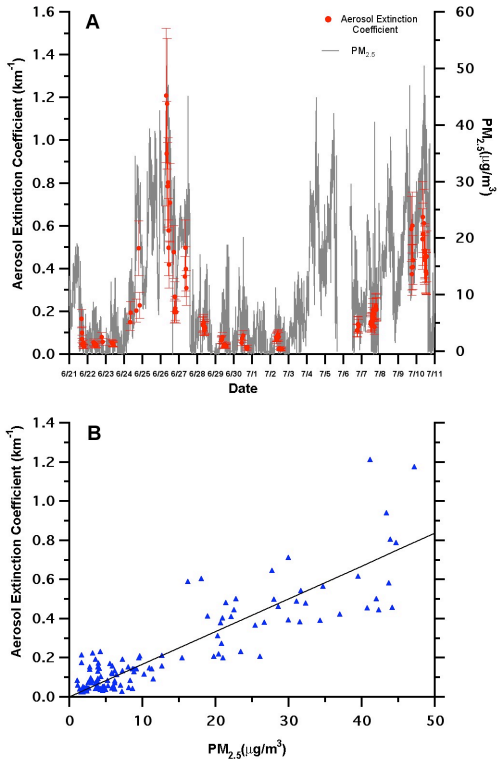

Fig. 6. Top panel **(A)** – aerosol extinction coefficient (red) and $PM_{2.5}$ (grey) at Ridgetown. Bottom panel **(B)** – $PM_{2.5}$ vs. aerosol extinction coefficient – Ridgetown. Slope of the trend line (y-intercept zero forced) = 53 μg m^{-3} km, $R^2 = 0.75$.

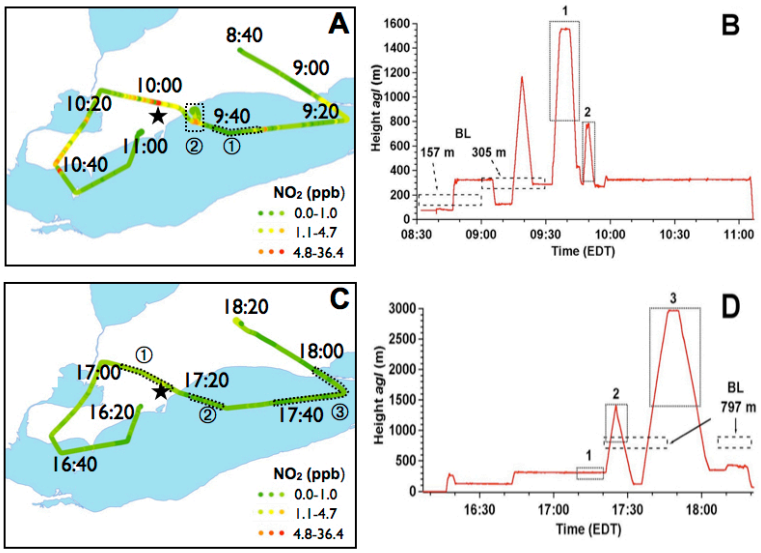

Fig. 7. AM flight path (08:32–11:07 EDT) and PM flight path (16:07–18:21 EDT) on 26 June 2007. Panel **(A)** and **(C)** show the NO_2 mixing ratios and the aircraft location every 20 minutes. Panel **(B)** and **(D)** show the aircraft elevation and BL (a.g.l.) as a function of time. The numbered sections on all figures show the locations, elevations, and approximate mixing ratios used for constructing the composite NO_2 profiles. The Ridgetown supersite location is starred.

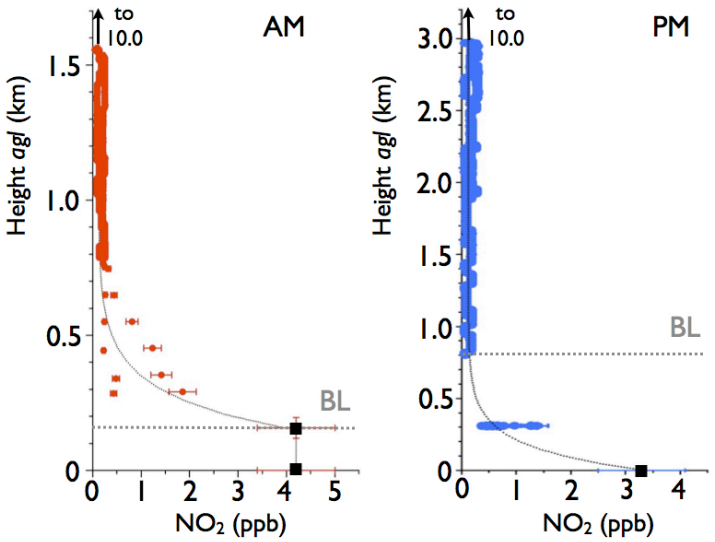

Fig. 8. NO_2 concentration profiles used to construct the composite NO_2 VCDs for the AM flight path (08:31–08:57 EDT-left) and PM flight path (17:52–18:10 EDT-right) on 26 June 2007. Colored circles represent NO_2 aircraft measurements, while black squares represent ground-based NO_2 by active DOAS. The boundary layer (BL) for each case is marked with the horizontal dashed line.

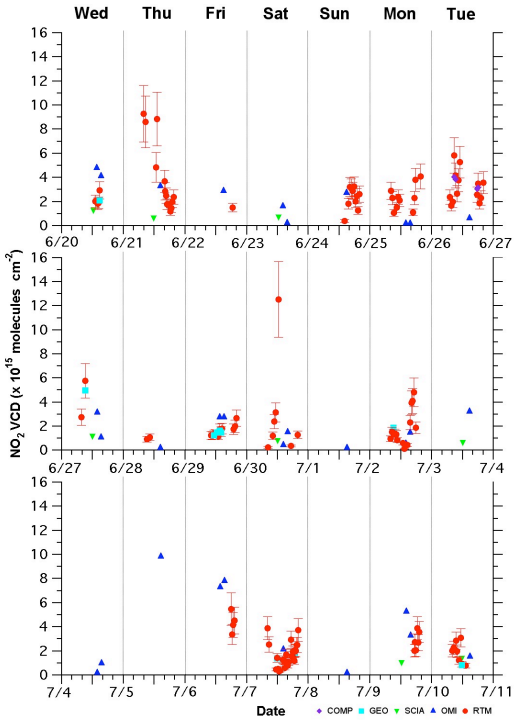

Fig. 9. Comparison of all NO_2 tropospheric VCDs at Ridgetown derived from aircraft/ground, satellite, and MAX-DOAS-RTM measurements.

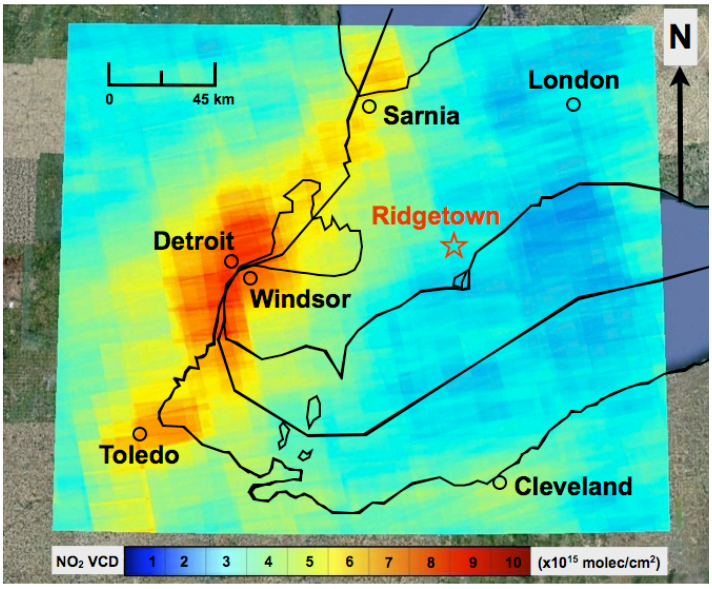

Fig. 10. Averaged OMI tropospheric NO_2 VCDs for the intensive field study period (10 June–10 July 2007) in southwestern Ontario. Ridgetown supersite is starred.

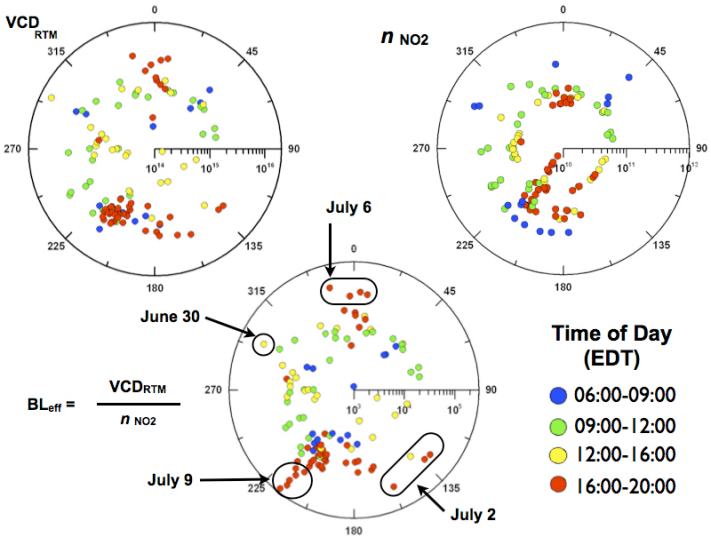

Fig. 11. Polar class scatter plot diagrams for Ridgetown. The NO_2 VCD_{RTM} (molec cm^{-2}), the NO_2 number density (molecules cm^{-3}), and the BL_{eff} (cm), are plotted on the radial axis vs. the wind direction, and are color-coded for the time of day of each measurement.

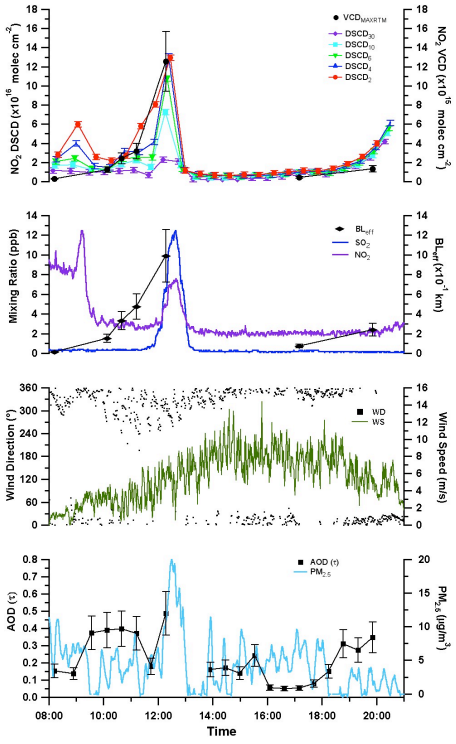

Fig. 12. Measurements at Ridgetown on 30 June 2007. NO_2 MAX-DOAS DSCDs with NO_2 VCD_{RTM} values are followed by ground level measurements of SO_2 and NO_2, BL_{eff}, wind direction, wind speed, $PM_{2.5}$, and AOD (τ_{RTM}).

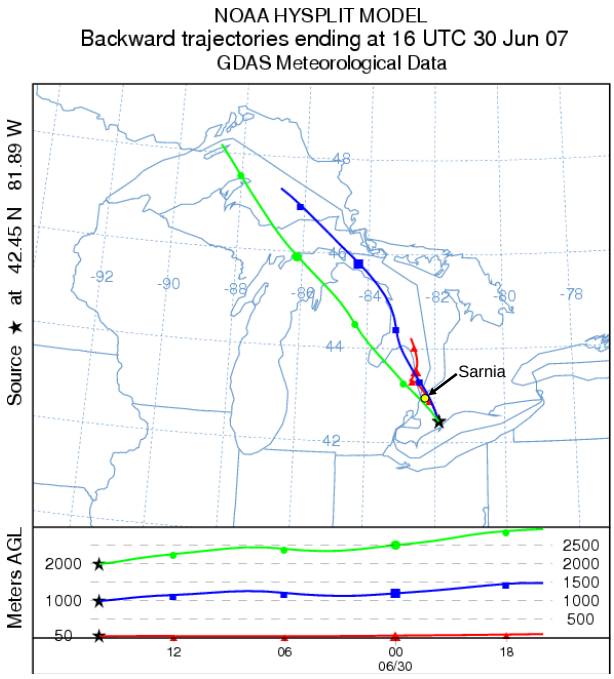

Fig. 13. HYSPLIT back trajectory for Ridgetown (starred) on 30 June 2007. Time scale in UTC.

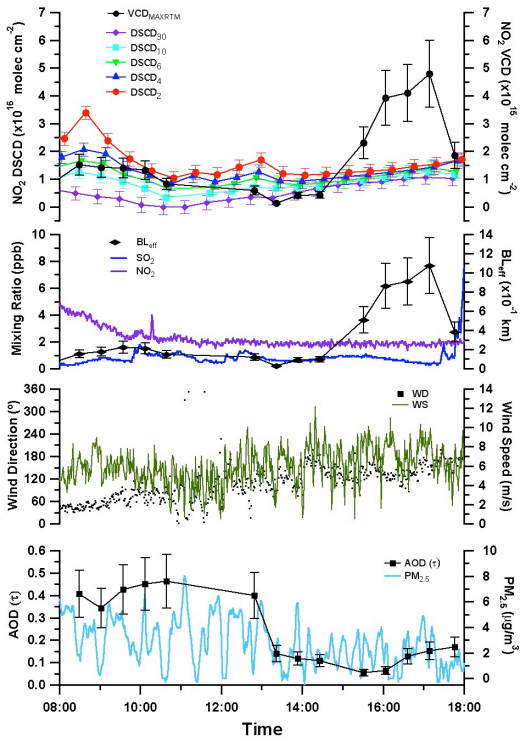

Fig. 14. Measurements at Ridgetown on 2 July 2007. NO_2 MAX-DOAS DSCDs with NO_2 VCD_{RTM} values are followed by ground level measurements of SO_2 and NO_2, BL_{eff}, wind direction, wind speed, $PM_{2.5}$, and AOD (τ_{RTM}).

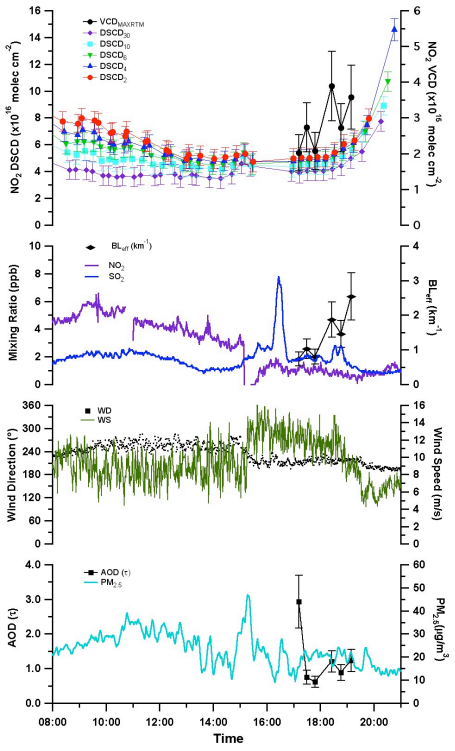

Fig. 15. Measurements at Ridgetown on 9 July 2007. NO_2 MAX-DOAS DSCDs with NO_2 VCD_{RTM} values are followed by ground level measurements of SO_2 and NO_2, BL_{eff}, wind direction, wind speed, $PM_{2.5}$, and AOD (τ_{RTM}).